Plasma Chem Plasma Process (2014) 34:403–441
DOI 10.1007/s11090-014-9545-1

ORIGINAL PAPER

A Model of Plasma-Biofilm and Plasma-Tissue Interactions at Ambient Pressure

C. Chen · D. X. Liu · Z. C. Liu · A. J. Yang · H. L. Chen · G. Shama · M. G. Kong

Received: 22 October 2013 / Accepted: 13 March 2014 / Published online: 4 April 2014

Abstract This paper presents the development of a model framework for plasma-biofilm and plasma-tissue interactions that can link molecular simulation of plasma chemistry to functions at a cell population level or a tissue level. This is aided with a reactive penetration model for mass transfer of highly transient plasma species across the gas–liquid boundary and a panel of electrical and thermal thresholds considering pain sensation, protein denaturation and lethal electric currents. Application of this model reveals a number of previously little known findings, for example the penetration of plasma chemistry into highly hydrated biofilms is about 10–20 μm deep for low-power He–O_2 plasma and this is closely correlated to the penetration of liquid-phase plasma chemistry dominated by O_2^-, H_2O_2, and HO_2 or O_2^-, H_2O_2, and O_3. Optimization by manipulating liquid-phase chemistry is expected to improve the penetration depth to 40–50 μm. For direct plasma treatment of skin tissues at radio frequencies, the key tolerance issue is thermal injuries even with a tissue temperature <50 °C and these can lead to induction of pain and protein denaturation at a small discharge density of 8–15 mA/cm^2 over few tens of seconds. These and other results presented offer opportunities to improve plasma-biofilm and plasma-tissue interactions. The model framework reported may be further extended and can be used to non-biomedical applications of low-temperature plasmas.

C. Chen · D. X. Liu (✉) · Z. C. Liu · A. J. Yang · M. G. Kong
Centre for Plasma Biomedicine, State Key Laboratory of Electrical Insulation and Power Equipment, Xi'an Jiaotong University, Xi'an 710049, People's Republic of China
e-mail: liudingxin@gmail.com

H. L. Chen · M. G. Kong (✉)
Frank Reidy Center for Bioelectrics, Old Dominion University, Norfolk, VA 23508, USA
e-mail: mkong@odu.edu

G. Shama
Department of Chemical Engineering, Loughborough University, Leicestershire LE11 3TU, UK

M. G. Kong
Department of Electrical and Computer Engineering, Old Dominion University, Norfolk, VA 23529, USA

Keywords Plasma medicine · Low-temperature plasmas · Biofilm interaction · Living tissues · Biophysics model

Introduction

Recent years have witnessed an increasing interest in studies of biological effects of near room-temperature ambient-pressure gas discharges (commonly known as cold atmospheric pressure plasmas or CAPs) [1, 2], some of which have already reached the stage of routine clinical use or successful phase-II clinical trials [3, 4]. A great deal of evidence has been reported of CAP-induced cellular effects such as microbial inactivation and apoptosis of cancer cells [1, 2], while much less is known of how plasma may effectively impact on microbes embedded in a biofilm and on cells growing in a tissue. Beyond the clinical arena, there are numerous other applications of CAPs including decontamination of polluted air and wastewater [5, 6], surface modifications to biomaterials [7, 8], and food and agriculture applications [9–11]. As the atmospheric pressure plasma technology is being advanced for biology and medicine, new and significant challenges are emerging. Two common questions from the user communities of CAPs are whether plasma-facilitated biomedical effects could be reproduced reliably, and how efficiently plasma agents may be transported into the depth of biofilms and living tissues. While obvious and logical, a satisfactory answer to these fundamental questions requires considerable advance beyond the current understanding.

Driven by electrons with a mean kinetic energy of a few electron volts, CAPs produce many types of reactive and modestly energetic agents such as charged particles, reactive species in ground, excited and metastable states, photons with energy typically below 6–8 eV (or wavelengths above $\lambda = 180$–200 nm), and thermal deposition typically having a characteristic gas temperature in a 300–400 K range. Heat fluxes and space-charge electric fields dynamically set up by the plasma are capable of exerting a physical force on cells and tissues [12–14], whereas reactive species and photons are often involved in a complex and evolving chain of chemistry of typically over 1,000 reactions [15–21]. These highlight a vulnerability to potentially cascading variations triggered by a small change in the physiochemical properties of the plasma, and hence to variations in the plasma's biomedical effects. Given the inevitable presence of liquid on and in living tissues, a further variation arises from the currently limited understanding of physics and chemistry of liquid-containing plasmas. Technological solutions are being developed to control factors affecting plasma interactions with cells and tissues, for example the rise of the gas temperature [22] and the change in the ambient gas composition [23]. At present however, such technology solutions alone are inadequate to ensure reproducible plasma-facilitated biomedical effects and to improve plasma access to cells embedded in biofilms and tissues. In this context, a critical knowledge gap is a quantitative framework with which to analyze, understand, and improve how low-temperature plasmas interact with biofilms and living tissues.

A central issue in plasma-biofilm and plasma-tissue interactions is concerned with mass and heat transfer as well as electrical penetration of plasmas into biofilms and tissues. Plasma penetration into biofilms and tissues, in terms of the transfer of chemically reactive species, heat, and electrical energy, is one of the most fundamental topics in plasma biomedicine, since it dictates how effectively plasma-induced cellular effects may be

reproduced in vivo and hence translated into therapeutic solutions. Biofilms are known to be a key mechanism of persistent infection and antibiotic resistance [24], whereas infected tissues and solid tumors impose considerable limit to penetration of antibiotics and anti-cancer drugs [25, 26]. Limitation mechanisms for drug penetration are however different in biofilms and in tissues. Highly hydrated with 69–93 % water content [27], a biofilm represents a considerable barrier to effective penetration of antimicrobial agents with the largest contribution being from catalytic reactions and minor roles being attributed to diffusion and sorption [28]. This is not dissimilar to a much-increased quenching rate of small reactive plasma molecules in liquid compared in atmospheric air. For example, OH radicals are detected in ambient air some 28 mm downstream from an atmospheric argon plasma using an UV cavity ring down spectroscopy [29] whereas in an aqueous environment they are known to be quenched within 10 nm. This similarity suggests that it is appropriate to explore and develop a diffusion–reaction model for description of plasma penetration into biofilms.

For penetration into living tissues on the other hand, the tissue structure and the cell membrane present significant restriction to the delivery of drugs and by large this could be mitigated only by the availability of pores and channels [30]. Even with smaller molecular weights, biologically significant plasma species are likely to be restricted similarly and need similar pores and channels for penetration. A more penetrating interaction of plasmas with tissues however is through electrical current and heat, as demonstrated recently in a series of excellent modeling studies of electric field propagating down wound-caused gaseous channels through living tissues [31, 32]. In the absence of plasmas, biological effects of electricity and heat are known, for example electroporation [33] and heat-induced pain [34], which may be studied from a starting point based on the Poisson and heat-transfer equations supported with experimental data [35]. A focus on electrical and thermal propagation into tissue is key to understand macroscopic penetration of electric current and heat delivered from CAPs to an intact mammalian tissue so as to understand the likelihood of pain and burn (tissue tolerance) and to examine the possibility of plasma-based hyperthemia. At present, these important issues have rarely been addressed in literature. The focus on electrical penetration will lay an important basis for future studies of electrically enabled membrane pore formation [30, 33] and indeed electrically modulated generation of reactive oxygen species (ROS) in cells and tissues. The latter is inspired by the fact that ion channels on the mitochondrial membrane are central to many cellular functions and their electrical modulation is directly related to production and loss of reactive oxygen species such as superoxide [36]. This suggests that electric field and reactive oxygen species may be directly related to each other intracellularly and in tissues without the involvement of ionized gases. With ROS and electric field being essential CAP constituents, CAP impact on mitochondrial membranes is of great interest to plasma physics and direct relevance to cell biology. It is therefore both desirable and feasible to establish a unified theoretical framework of quantitative description of how electrical, thermal, and chemical effects of CAPs are transported into biofilms and tissues, and how these transport properties may be translated to cell and tissue functions.

This study aims to provide a model framework of quantitative description for plasma interactions with biofilms and tissues from the first principle aided with experimental data when possible, with a focus on how plasma induced electrical, chemical and thermal effects may propagate into biofilms and tissues. For biofilms at the first glance, this appears to be a classic mass transfer problem between two fluids [37] albeit with underpinning chemical reactions, the participation of moving ionic species, and a possible presence of an electric current. Yet a close look reveals the dominant role of transient chemical reactions

in CAPs with timescales as short as nanoseconds. A central question is how knowledge of plasma mass transfer may be related to the efficacy of microbial inactivation. The need to link to tissue function (e.g. pain and injury) is similar in the case of tissues. In this study, we will consider three regions, namely the plasma-generation region, an interfacial region between the plasma region and a biological sample, and the biological sample region (i.e. either a biofilm or a tissue). Reactions and transport of plasma-produced reactive molecules are considered when mass transfer is possible (i.e. in the case of biofilms), whereas biomolecular and cellular effects are indirectly included using either biophysical models or experimental data. Electrical fields set up by an external voltage and space charges are considered for all three regions, and thermal effects are considered for plasma-tissue interactions given the connection to hyperthermia and thermal dose control against burn [38, 39]. A model based on the above premises should be appropriate for investigations of (1) penetration and evolution of plasma chemistry into biofilms and (2) electrical field and temperature profiles through skin and into subcutaneous tissues with direct implication of electrical and thermal tolerance. There is a large body of computational molecular biology [40] and computational system biology [41], some supported experimentally, and such models can indeed be added to the theoretical framework reported here at a future point. This work represents a first attempt to develop a quantitative framework capable of analyzing existing experimental evidence of plasma interactions with biofilms and tissues and extendable to include suitable models of neighboring scientific subject areas.

In section "Model Development", the model and its development are detailed, beginning by placing the importance of this work in a historical context, for both plasma-biofilm and plasma-tissue interactions. A particular focus is placed on how mass transfer of plasma species through the gas–liquid boundary may be modeled with highly transient chemical reactions and how macroscopic electric and thermal fields may be related to tissue functions. Justifications based on either comparison with experimental data or existing models of biofilms or tissues are provided when appropriate, whereas aspects in the model for future improvement are also discussed. With the model established, results of plasma penetration into biofilms are represented in section "Result and Discussion" with a focus on chemical reaction chains underpinning main plasma species and **in** comparison with existing experimental data of plasma inactivation of biofilm-forming bacteria. Also presented in Section "Result and Discussion" are results of plasma-tissue interactions with a focus on electrical and thermal tolerance. Finally discussions and conclusions are summarized in section "Concluding Remarks". The quantitative model reported here is aimed at biomedical applications, but should be useful for plasma treatment of wastewater [6] and plants [9].

Model Development

Historical Note

The importance of a quantitative description for plasma interactions with biological matters is best illustrated by the experience of the first era of the plasma biomedicine research between 1900 and 1980's. The then central question was whether negative air ions, almost inevitably produced by ambient pressure gas discharges, may have biological effects particularly on human health [42–44], and the interest was stimulated by the award of the 1906 Nobel Prize in Physics to JJ Thomson for the discovery of the conduction of electricity in gases. Initial studies using animals were gradually replaced by the use of the

simpler life form of bacteria [45, 46]. However scientific studies before 1960's were primitive without adequate control of experimental conditions and without the full benefits of molecular biology. This formed an unfortunate marriage with an overenthusiasm of air ion generator manufacturers, leading to a few tens of claims including reduced bacterial and fungal growth, decreased cancer cell growth, increased healing of ulceration as well as improvement of learning and cessation of pain from burns [47]. Where some of those claims have been confirmed at a molecular level or/and in randomized clinical trials much later during the current era of plasma biomedicine (from 1990's onwards) [3, 4, 48–52], many were then little substantiated and suffered from inconsistency and irreproducibility. This led to controversies and eventually a FDA sanction on sales of all air ion generators in 1950's [47].

Scientifically it was fortunate that several large research programs were able to continue post 1950's. An example was the work of Krueger and co-workers at UC Berkeley. They used an ambient air corona discharge, an example of which is shown in Fig. 1, to study its treatment of a downstream bacterial sample. Their studies highlighted several aspects of the prevailing experimental protocols that may have contributed to the inconsistency of results before 1960's, and these included [53]:

(1) neglect of the role of neutral species such as ozone and oxides of nitrogen (i.e. plasma chemistry);
(2) failure to measure and control ion density, gas temperature and environmental humidity (i.e. detailed plasma diagnostics and local environment control);
(3) failure to control variation in ion density due to ambient particulates and gas pollutants (i.e. local environment control);
(4) failure to ground the sample leading to a time dependent increase of electrostatic field of deposited charges.

In fact, they went on to study long-term effects of air ions and other plasma species from corona discharges on rats and mice [46]. These studies have laid a valuable foundation of scientific substances for today's plasma biomedicine research. The current endeavors for biomedical applications of low-temperature gas discharges are in a much better position also because of scientific advances made elsewhere, for example the technological breakthrough for stable ambient pressure plasmas [55], the substantial advance in low-temperature plasma physics in terms of both laser diagnostics and large-scale computer simulations [56], and full establishment of molecular biology [57]. Critically, FDA and the regulatory bodies in Europe have since 1980's approved several plasma-based technologies [3, 58, 59]. Nevertheless, the historical lesson discussed above should motivate a critical diligence of achieving robust reproducibility of plasma-facilitated biological effects. In this context, it is highly desirable to acquire an ability for quantitative analysis of plasma-cell and plasma-tissue interactions to aid their control, monitoring and improvement.

Plasma-Biofilm Interaction Model

Three regions are involved in plasma-biofilm interactions, namely the gaseous plasma generation region (i.e. a gas bulk), the biofilm region modeled as a semi-infinite liquid bulk, and the gas–liquid boundary region as shown in Fig. 2. A plasma-biofilm interaction model needs to accurately describe mass transfer together with related chemical processes within each region as well as those cross the gas–liquid boundary. For the biofilm and for the gas–liquid boundary however, existing models tend to consider solutes with much less

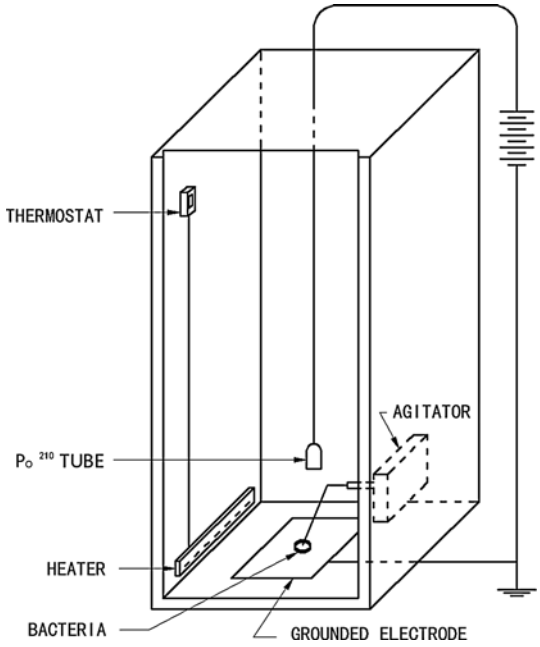

Fig. 1 An example of apparatus used during 1950's to study the effects of low-temperature atmospheric pressure plasmas (an ambient air corona discharge in this case) on living systems (bacteria in this case). Variations in the sample conditions and in the plasma-sample interactions were known to have a significant impact on experimental results. Here, the reactor cage was used to minimize variation in the ambient gas, and the thermostat-controlled heater to control the sample temperature and also the effects of moist. The sample was also grounded to mitigate a time-dependence of charge accumulation. Reproduced from Ref. [54] with permission of the Rockefeller University Press

reactivity than reactive plasma species and therefore their direct applicability to Fig. 2 must be re-examined in light of the very transient nature of plasma reactions. For mass transfer through a gas–liquid boundary, the majority of the current models usually assume that the mass transfer is through a thin boundary layer sandwiched between a gas bulk and a liquid bulk, with their molecular transfer limited mainly by diffusion and their chemical reactions, when present, having secondary effects [60–62]. Although no assumption should be made of a sharp line of demarcation between a bulk fluid and the boundary layer [60], the two bulk fluids and the boundary layer are nevertheless considered to have distinct different characteristics. This encourages, at this early stage of theoretical development, an approach of a compartmental modeling than integrated modeling [60–62]. The approach proposed for the plasma-biofilm interaction is to model the plasma and the biofilm regions separately, to develop a mass-transfer model for the gas–liquid boundary region, and finally to link them together through appropriate boundary and constrain conditions.

Gas Bulk Region

The gas bulk region (i.e. the plasma generation region) can be well characterized by a fluid treatment with a comprehensive account for the mass and heat transfer in the space between the two electrodes, the underpinning electron kinetics, and the related plasma chemistry. Here, the gas discharge is sustained between two parallel electrodes having an atmospheric pressure He–O_2 gap of 2 mm and excited at 13.56 MHz and 40 W/cm^3. The power density chosen is not untypical experimentally, and the O_2/He ratio = 0.1–10 %. For a plasma-on timescale of no more than 60 s at 40 W/cm^3 (a common timescale for plasma treatment of biological samples), plasma-generated heat does not give rise to too much an increase in the gas temperature when the electrodes are cooled with circulating water. This is a reasonable first approximation as thermal dehydration of a biofilm could lead to a reduction of biofilm

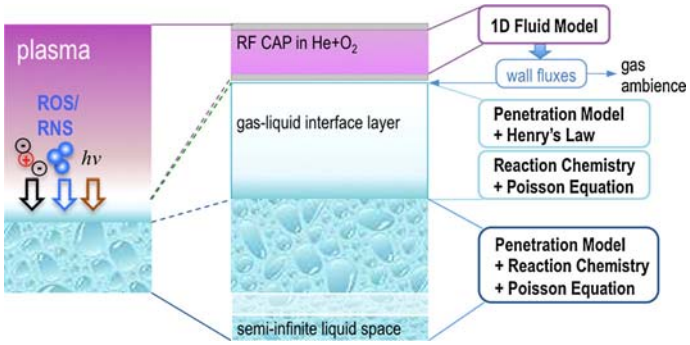

Fig. 2 A plasma-biofilm interaction model with the highly hydrated biofilm modeled as a liquid bulk of infinite depth and separated from the modeling of plasma generation and the gas–liquid interfacial layer. Wall fluxes of reactive and other plasma species obtained from the 1D fluid plasma model are used as the input parameters for the liquid phase modeling (including the interfacial layer). For the liquid phase, a modified penetration model is used with account of chemical reactions and a spatially evolving electrostatic field of drifting charged plasma species, for the interfacial layer (pressure balance modeled with Henry's law) and the liquid bulk

porosity and so compromised plasma penetration. Inclusion in the model of gas temperature calculation is feasible and will be considered for future studies. This is expected to have modest influence on the concentrations of plasma species but the overall pattern of gas-phase plasma chemistry. The simulation of plasma generation and dynamics is based on a one-dimensional fluid model using a diffusion-drift approximation [63], aided with direct experimental validation [64, 65] and being comparable to other fluid models of CAPs [66–68]. The diffusion-drift assumption of the fluid model is based on the fact that the collision frequency of CAPs is much higher than its driving frequency and the mean-free path length is small compared to the Debye length [69]. The electron energy distribution function is obtained by solving the Boltzmann equation with BOLSIG+. The fluid model is supported favorably by direct comparison between results of the diffusion-drift approximation and those of kinetic simulation for radio-frequency microplasmas [68, 69], and therefore it can reliably describe electron kinetics and dynamics.

To adequately include reaction chemistry in the fluid model, a global model is used to screen and rank chemical reactions in terms of species concentrations and the significance of a given plasma agent in the reactions it participates [70, 71]. Plasma species and relevant reactions thus selected are then used in the one-dimensional fluid model and iterations are taken place between the global and the fluid model to ensure no unjustified omissions [63, 72]. The plasma chemistry model includes 21 plasma species and 267 chemical reactions between them, identical to those considered and detailed in Ref. [70]. Wall fluxes of relevant plasma species onto the liquid-facing electrode are assumed to leave the gas bulk without loss, and at O_2/He = 1 % the time-averaged concentrations and the wall fluxes are given in "Appendix 1" (the first three columns). The gas phase simulation is performed independent of the two other regions (i.e. the gas–liquid boundary region and the liquid bulk), as an approximation and assuming little participation of vaporized species in plasma chemistry. This scenario can be realized in practice by operating at low electrical power density and adding a gas diffusion buffer region between the liquid-facing electrode and the liquid surface. The effect of water vapor itself is considered in the gas–liquid boundary region.

Liquid Bulk Region

A liquid bulk may be used to model biofilms [73], given their highly hydrated state with a water content to be 69–93 % [27]. It is known that the transport of small solutes through a biofilm is dominated by diffusion and to a lesser extent by chemical reactions and with sorption playing a negligible role [73]. Such solutes may be directly modeled involving complex reactions with cellular components (e.g. proteins) and extracellular components [40]. However they may also be modeled indirectly by introducing the concept of effective diffusion coefficients, D_e, by comparing the diffusion coefficient of a given solute in pure water (D_{aq}) to an experimentally derived diffusion coefficient for the solute [74]. The relative effective diffusion coefficients, D_e/D_{aq}, vary between 0.2 and 0.8 with ammonium at 0.8, oxygen, nitrate, and nitrous oxide at 0.6–0.7, and sucrose and glucose at 0.2–0.3 [73]. Reduction in the diffusion coefficient from its value in pure water is within one order of magnitude [74, 75], reflecting modest reactivity for solutes typically associated with biofilms and their antibiotics, and this is fundamental to the concept of an effective diffusion coefficient. By contrast, reactive plasma species can have much shorter lifetimes with the timescale of electron impact reactions, charge transfer and recombination, and neutral reactions in the gas phase ranging from a few tens of nanoseconds to a few tens of microseconds. These are at least 3–4 orders of magnitude below a typical diffusion timescale of a few seconds over a distance of a few millimeters [19]. In the liquid phase, reaction timescales of plasma species are expected to be even shorter [29, 76] and the diffusion timescale longer. The use of an effective diffusion coefficient is likely to deemphasize or even remove the role of short-living species (e.g. O/O*, O_2*, OH), even though it may be reasonable for long-living species such as H_2O_2 and O_3. This suggests that a diffusion–reaction model is both appropriate and necessary. Importantly, production and loss of many plasma species are characteristically interwoven together and little is at present understood of how a small group of desirable plasma species (for biological effects) may be produced, lost, and transported in liquid. As plasma species are transported through a hydrated biofilm, short-living plasma species are dropping out of the in-liquid plasma chemistry resulting in either a boost or a reduction in their support to the generation of longer-living species. Also liquid-phase reactions unsupported in the gas phase may kick in both to enhance penetration of decaying short-living species and, more importantly, to create liquid-phase reactants (e.g. OH and HO_2). These and other interwoven generation/loss pathways in the liquid phase must be delineated by directly including relevant chemical reactions in the model. Finally drift due to the electric field of penetrating charged particles needs to be considered also.

Here, the liquid bulk is assumed to have a thickness of 10 mm, much larger than the typical thickness of a biofilm for the liquid bulk to be treated as semi-infinite. With a diffusion–reaction model for the liquid bulk, the transport of plasma agents with ongoing chemical reactions between them and with water molecules is given by

$$\frac{\partial C_{i,l}}{\partial t} = D_{i,l}\frac{\partial^2 C_{i,l}}{\partial x^2} + \Sigma R_{i,l} \tag{1}$$

where $C_{i,l}$ is the concentration of the element i, $D_{i,l}$ is its diffusion coefficient in the liquid, and $R_{i,l}$ the rate of chemical reactions associated to the element i (subscript l is denoted to liquid). The flux of the element i is

$$\Gamma_{i,l} = -D_{i,l}\frac{\partial C_{i,l}}{\partial x} \tag{2}$$

However the above description does not apply to cases where an element is electrically charged and the charged element is also driven by a space-charge electric field set up by all charged elements in the liquid bulk. With charged species taking into account, the flux of a charged element now has two terms, one due to diffusion $\Gamma_{i,diff}$ and the other due to drift $\Gamma_{i,drift}$, or mathematically [77, 78]

$$\Gamma_{i,l} = \Gamma_{i,diff} + \Gamma_{i,dirft} = -D_{i,l}\nabla C_{i,l} + z_i\mu_{i,l}C_{i,l}F\vec{E}/N_A \tag{3}$$

where z_i and μ_i are respectively the ion charge number and the mobility of the charged element, E is the electric field, and F and N_A are respectively the Faraday constant and the Avogadro constant. As a result, Eq. (3) becomes

$$\frac{\partial C_{i,l}}{\partial t} - \nabla\cdot(-D_{i,l}\nabla C_{i,l} + z_i\mu_{i,l}C_{i,l}F\vec{E}/N_A) = \Sigma R_{i,l} \tag{4}$$

The electrostatic field established by charged elements is solved from the Poisson equation:

$$\frac{\partial E}{\partial x} = \Sigma z_i e C_{i,l}/\varepsilon \tag{5}$$

with ε being the permeability of the liquid and F/N_a having been replaced with the electron charge e. Liquid-phase chemistry is described with 19 species (e, O^-, O_2^-, O_3^-, OH^-, HO_2^-, H^+, O, O(1d), O_2(a), O_2, O_3, H_2O, H, H_2, HO_2, HO_3, OH, H_2O_2) and 84 chemical reactions among them (see "Appendix 2" and references therein [79–83]). He species in both metastable and charged states are not included due to their low fluxes and their escape from the boundary region due to the lightness of helium. It is worth noting that rate coefficients of aqueous reactions involving electrons are obtained from reported electrolysis experiments [79] rather than from exact formula that depend on electron energy. This is because rates of liquid-phase reactions involving low-energy electrons of 0.1–5 eV are scarce [84] and the effects of modestly energetic electrons in liquid are not fully understood [85]. For the study reported here, electron impact reactions in liquid with electron energy dependent rate coefficients are not directly accounted for nor considered to be critical at this stage, partly because electrons entering the liquid have much lower kinetic energy than in the plasma-generation region and the threshold electron energies for dissociation and ionization are much higher in liquid than in gas. Similarly, effects of photons are not considered since photon emission is not strong in He–O_2 plasmas [86] and photon absorption is likely to be significant in the gas buffer region between the liquid-facing electrode and the gas–liquid boundary. Nevertheless the model based on Eqs. (1)–(5) does not preclude future inclusion of the effects of modestly energetic electrons and photons when rate coefficients of relative reactions involving them become available and fully established.

To solve the above equations, diffusion coefficients of liquid-phase species are listed in "Appendix 3". To link to mobility, we note that diffusion coefficient of a particle in a liquid depends on its radius, r_i, the viscosity of the liquid, η_l, and the liquid temperature T_l, and is given by [87]

$$D_{i,l} = kT_l/6\pi r_i\eta_l \tag{6}$$

where k is the Bolzmann constant. Using the Nernst-Einstein equation [88], the drift velocity of an ionic species may be obtained from

$$\mu_{i,l} = z_i e D_{i,l}/kT_l \tag{7}$$

For the liquid-phase species, their diffusion and mobility coefficients are listed in "Appendix 3" with their source references. At the gas boundary of the liquid bulk, concentrations of neutral and charged elements at the gas–liquid boundary need to be supplied as the boundary condition parameters from the simulation for the gas–liquid boundary (see discussion in section "Gas–Liquid Boundary Region"). These boundary conditions are discussed and provided in Section "Boundary Conditions".

Gas–Liquid Boundary Region

For CAPs in contact with liquid, mass transfer across the gas–liquid boundary has been modeled zero-dimensionally using a simple film model with an assumed film thickness [89] and using a characteristic timescale of mass transfer [90], both with simple phenomenological plasma chemistry. A more recent study introduces a fuller plasma chemistry using a global model also in zero dimension [91]. Though informative, zero-dimensional treatments are in general inadequate to describe mass transfer. One-dimensional or multi-dimensional descriptions of mass transfer across a boundary of a gas discharge with a static and unstirred liquid has scarcely been reported in scientific journals so far, though discussed at very recent scientific conferences [92]. Without the involvement of gas plasmas, mass and heat transfer between two phases (e.g. gas and liquid) is well studied, particularly in chemical engineering and astrophysics. Two classic theories of mass transfer between two phases are the film model and the penetration model [93–105], though the surface renewal model [106] and the film-penetration model are also used [107]. The film model assumes that steady-state molecular transfer is controlling over an often fixed distance (e.g. a stagnant film) [93, 94], whereas the penetration theory assumes that the boundary region is continuously replaced by eddies and that an unsteady state molecular transfer into the eddies controls mass transfer across the boundary over a finite timescale [62, 105]. In the latter case, physical stirring of the liquid is usually needed to ensure continuous replacement of eddies. Chemical reactions and ionic species can be factored in, though reaction chemistry considered so far in these plasma-free mass transfer models is normally regarded to have little contribution to eddy mixing and rarely has a timescale as short as a few tens of nanoseconds.

Direct application of existing mass transfer models is unlikely to be appropriate for plasma species transfer across the gas–liquid boundary, due to the very wide range of timescales of chemical reactions in plasmas. The classic film theory requires a relatively thick boundary region over which the mass transfer can be regarded to be at a constant velocity and in a steady state [108]. Yet as shown below in "Result and Discussion", some plasma species (e.g. O and O_2^*) are extremely transient with nanosecond lifetimes in liquid [71] and some (e.g. hydrogen peroxide) can be transported without much loss even after a centimeter depth. These suggest a non-equilibrium and non-steady mass transfer. Plasma species of very different lifespans are also closely coupled with each other in their generation and loss. Therefore it is inappropriate to force one length-controlled film (i.e. one stagnant film) to capture the transport of reactive species of very different lifespans. On the other hand, the use of the classic penetration model requires normally the liquid surface to be well stirred physically to ensure good mixing between the transported solutes and the liquid, but the physical stirring is usually absent in a plasma-biofilm interaction. As discussed above however, chemical reactions of plasma species in the liquid is very rapid and the low concentrations of transported plasma species, compared to the water molecule concentration, lead to their rapid dissolution with water. This suggests that a good mixing of plasma species with the liquid may in fact be achieved chemically and through rapid

dissolution, thus offering support to possible use of a penetration model with the caveat that a good mixing is achieved chemically without physical stirring. Given the above considerations for a penetration theory, the mass transfer of plasma species across the gas–liquid boundary should take the following mathematical format:

$$\frac{\partial C_i}{\partial t} = D_i \frac{\partial^2 C_i}{\partial x^2} \tag{8}$$

The thickness of the unsteady boundary region is not fixed and is obtained from the solution of Eq. (8). It should be mentioned that no subscript is used here to denote gas or liquid as the boundary region is dominated by water vapor.

It is important to assess how rapid chemical reactions may influence incoming plasma species on the gas–liquid boundary. Before gaseous plasma species enter into the liquid phase, they are subject to reactions with water vapor near the liquid surface and also to re-balance of partial gas pressure (e.g. O_2, O_3 and H_2O for example) according to Henry's law [96, 97]. As liquid molecules are saturated in the liquid phase, we assume that water molecules vaporizing from the liquid to the gas regions are also saturated near the boundary surface. In other words, the concentration of the vapor water molecules is very high in the gas–liquid boundary layer. On the gas side immediately next to the liquid surface, a narrow region of a He + O_2 + H_2O plasma afterglow is likely to form. According to a recent global simulation of plasma chemistry in He + O_2 + H_2O mixture [71], charge transfer reactions take place to produce ionic water clusters, such as $O_2^+ \cdot (H_2O)_{n=1-2}$ and $O_3^- \cdot (H_2O)_{n=1-2}$, on the gas side of the boundary surface, for example

$$\begin{aligned}
&O_2^+ + H_2O + M \rightarrow O_2^+ \cdot H_2O + M;\ O_4^+ + H_2O + M \rightarrow O_2^+ \cdot H_2O + O_2 + M \\
&O_2^+ \cdot H_2O + H_2O \rightarrow H_2O^+ \cdot H_2O + O_2; O_2^+ \cdot H_2O + H_2O + M \rightarrow O_2^+ \cdot (H_2O)_2 + M \\
&H_2O^+ \cdot H_2O + H_2O \rightarrow H^+ \cdot (H_2O)_2 + OH; O_2^+ \cdot (H_2O)_2 + H_2O \rightarrow H^+ \cdot (H_2O)_2 + OH + O_2
\end{aligned} \tag{9}$$

These water clusters become dominant ions even with low water vapor content of [H_2O]/[He + O_2 + H_2O] = 1 %, whereas nonhydrated O_4^+ and O_3^-, dominant ions in He + O_2 plasma [70], have diminishing concentrations with increasing water content [71]. At higher water vapor content above 2 %, the after-glow plasma behaves very much like a He + H_2O plasma [71] and the dominance of ionic water clusters is likely to hold true in plasmas generated in O_2 + H_2O diluted with other inert gases also [91]. Timescales of charge transfer reactions involving plasma species are microseconds in the gas phase and much shorter in the presence of water vapor. Hence chemical reactions of incoming plasma species with water vapor near the gas–liquid boundary are rapid and dominated by ionic water clusters. These reactions take place in a narrow gas film on the gas side of the gas–liquid boundary, and this gas film is referred to as *the reactive gas film* in order to be distinguished from the stagnant gas film concept used classically for mass transfer via diffusion [93].

Leaving the reactive gas film and entering the liquid surface, hydrophillic proton-containing water clusters are easily and quickly dehydrated to release hydrogen ions through $H^+ \cdot (H_2O)_{n=1-7} \rightarrow H^+ + nH_2O$. This takes place in a very narrow region on the liquid side of the gas–liquid boundary, and this process may be likened to absorption similar to how CO_2 is absorbed onto an aqueous surface [98]. This narrow region may be conveniently referred to as *the liquid absorption film*. Similarly, negative charged water clusters such as $O_2^- \cdot (H_2O)_{n=1-2}$ and $O_3^- \cdot (H_2O)_{n=1-2}$ [71] may also be considered to be

absorbed through dehydration after entering the liquid bulk and thus being released to form O_2^- and O_3^-. Absorption is known as a way for mass to escape the gas phase, and the rate of change of an absorbed gas agent on a gas–liquid interface area A is proportional to the difference in its concentration at the gas phase and at the absorbance point, or [60]

$$\frac{dC_{i,l}}{dt} = D_{i,l}(C_{i,g} - C_{i,l})/A \tag{10}$$

where $C_{i,g}$ and $C_{i,l}$ are respective the concentration of species i in the reactive gas film and in the liquid side of the boundary layer. The left hand side of Eq. (10) is identical to the left hand side of Eq. (8), suggesting that absorption of hydrated plasma species may be modelled in the same theoretical framework as the penetration of nonhydrated plasma species. In fact, the absorption model is often regarded as a special case of the penetration theory.

It is now evident that the gas–liquid boundary region is conceptionally modelled here with a reactive gas film and a liquid absorption film, each on one side of the liquid surface and truncated together to bridge the gas bulk and the liquid bulk. Given the dominant role of rapid chemical reactions distinctively different from those typical in chemical engineering, the model described in Eqs. (1)–(10) is perhaps best described as a *reactive penetration model*. Though the thickness of the reactive gas film is indefinite and that of the liquid absorption film also needs to be estimated, it is of interest to first discuss the length scale of the gas–liquid boundary region consisting of both the gas and the liquid films. Assuming the water vapor concentration $[H_2O] = 5.36 \times 10^{23} m^{-3}$ in air, corresponding to 2.3 % (reasonable for saturated water vapor in atmosphere at 300 K), the lifetimes of O_2^+ and O_4^+ may be estimated from their reactions with water molecules (see (9) and data from [109, 110]) and these are found to be 0.27 and 1.09 ns respectively. Thus their diffusion distance may be estimated from their diffusion coefficient D (data from [63, 111]) as $\Delta d = (D \cdot t)^{1/2}$ and are found to be 0.12 and 0.23 μm for O_2^+ and O_4^+, respectively. This highlights that chemical reactions and mass transport events in the gas–liquid boundary region already become significant on a nanosecond scale in time and a submicrometer scale in length.

In principle, chemical reactions, diffusion, and dehydration may be modelled for the gas–liquid boundary region using a one-dimensional model. This is at present likely to be premature and may force largely assumed reaction and transport parameters, since considerable uncertainties exist over the transport parameters of ionic water clusters, the rates of the charge transfer reactions of (9), and the dehydration rates of ionic water clusters. Although the global model simulation of [71] may be alternatively used, zero-dimension treatments are fundamentally unsuited for mass transfer. Therefore the gas–liquid boundary region is treated here with an assumption of instantaneous mass transfer, justified with the nanosecond timescale of relevant mass transfer events. As an approximation, we assume that all non-hydrated species can largely maintain their fluxes exiting the liquid film as entering the gas film. They are listed in "Appendix 1" (columns 4–6) for O_2/He = 1 % in terms of their fluxes and, if appropriate, their concentrations from the gas bulk, through the gas film, to the liquid bulk. Exceptions are for long-living species of O_2, H_2O and O_3 whose concentrations at the liquid surface is subject to Henry's law (see details in Section "Boundary Conditions"). Helium metastables and ions have very low fluxes compared to others and are likely to undergo a diffusion back to the gas phase because of their light weight. They are therefore ignored for the simulation of the liquid bulk. For hydrated species, it is reasonable to assume that the charge transfer reactions of (9) in the gas film and the dehydration in the liquid film are highly efficient with little loss such that $\Gamma_{O2+,g} = \Gamma_{H+,l}$ may be supported. This assumption is examined in Section

"Result and Discussion". Taken together, the reaction-penetration model is illustrated in Fig. 3 with boundary and constrain conditions as well as its link to the fluid model of the gas bulk and the diffusion–reaction model of the liquid bulk.

Boundary Conditions

Assuming the liquid surface is at $x = 0$ and the liquid bulk ends at $x = d_0 = 10$ mm. We consider first the boundary conditions for both ionic and neutral species. At $x = d_0$, all transferred plasma species, both neutral and ionic, are assumed to have reached their steady-state value:

$$D_{i,l}\frac{\partial C_{i,l}}{\partial x}|_{x=d_0} = 0 \tag{11}$$

$C_{i,l}$ is the concentration of species i in the liquid side of the boundary layer and $D_{i,l}$ is its diffusion coefficient in the liquid phase. At $x = 0$ on the other hand, ionic species and electrons have low concentrations and their passage through the boundary layer is very fast (i.e. on a nanosecond timescale), suggesting that they are unlikely to either accumulate or lose in the boundary region. Therefore the gas-phase flux of a charged species, $\Gamma_{ic,g}$, may be considered to remain unchanged at the liquid side of the boundary layer, or mathematically,

$$\Gamma_{ic,g}|_{x=0} = \left(-D_{i,l}\frac{\partial C_{i,l}}{\partial x} + z_i e\mu_{i,l}EC_{i,l}\right)\Big|_{x=0} \tag{12}$$

where $\mu_{i,l}$ is the mobility of species i in the liquid bulk.

Similarly for reactive neutral plasma species such as O, O(1d) and O_2(a) (but not O_3), their reactions with water molecules are very frequent. It is therefore reasonable to assume that their concentrations in the liquid is far from saturated and that the flux of a reactive neutral species is the same on both sides of the liquid surface. Or,

$$\Gamma_{i,g} = -D_{i,l}\frac{\partial C_{i,l}}{\partial x}|_{x=0} \tag{13}$$

For neutral species that are insufficiently reactive to be significantly involved in chemical reactions in the gas–liquid boundary layer including O_2, H_2O and O_3, their transfer across the gas–liquid boundary may be discribed with the following boundary conditions [60, 62, 106]:

$$k_{i,g}(C_{i,g} - H_i C_{i,j}|_{x=0}) = -D_{i,l}\frac{\partial C_{i,l}}{\partial x}|_{x=0} \tag{14}$$

where $C_{i,g}$ is the concentrations of species i in the gas side of the boundary layer, $k_{i,g}$ is the transport rate in the gas phase, and H_i is its dimensionaless Henry's coeffficent. The left hand side of eq.(14) represents the resistance to the gas–liquid transfer, and the right hand side represents the net flux of the transferred species i into the liquid, Γ_i. In the extreme case of little resistance, the transport rate may be regarded as infinite and Eq. (14) is then simplified to a boundary condition at $x = 0$:

$$C_{i,g} = H_i C_{i,l} \tag{15}$$

At the beginning of mass transfer to the liquid surface, $t = 0$, the concentration of the transferred species i at $x = 0$ in the liquid phase is zero and therefore this leads to the following formula of the transport rate

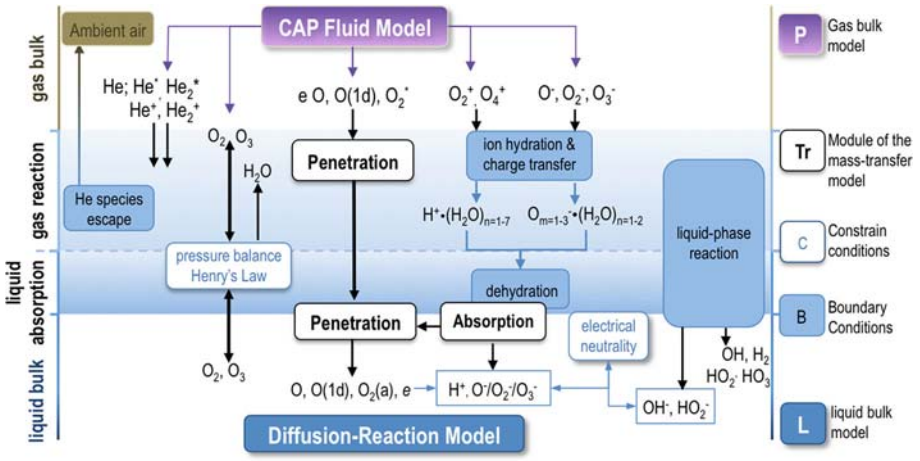

Fig. 3 The reaction-penetration model for mass transfer through the gas–liquid boundary, and its link to the fluid model for the gas bulk (marked with a *purple box*) and the diffusion–reaction model for the liquid bulk (for biofilm, marked with *dark blue box*). The mass-transfer model has a few components, marked with *white box* and *black text*. Constrain conditions for the balance of partial gas/vapor pressures and for the electrical neutrality between positive and negative ions are marked with *white box* and *blue text*; and hydration, other liquid-phase reactions, and dehydration are marked with *light blue boxes* (Color figure online)

$$k_{i,g} = \Gamma_i / C_{i,g} \tag{16}$$

The boundary condition is therefore (also illustrated in Fig. 3):

$$\Gamma_i \left(1 - H_i \frac{C_{i,l}}{C_{i,g}}\right)\Big|_{x=0} = -D_{i,l} \frac{\partial C_{i,l}}{\partial x}\Big|_{x=0} \tag{17}$$

Equations (12), (13), (17) are respectively the boundary conditions at $x = 0$ for charged species, reactive neutral species and non-reactive neutral species.

For initial conditions at $t = 0$ when the plasma species are about to reach the liquid surface, their concentrations need to be specified. For the studies reported here, the pH value of the liquid is assumed to be seven and the liquid temperature is at room temperature. This is an approximation, since treatment of a liquid sample such as a biofilm by low power atmospheric pressure helium–oxygen plasmas usually leads to little change to the pH of the liquid sample [112, 113]. However it is worth noting that plasma treatment at higher power can change the pH of the sample markedly [113] and also biofilms are known to support pH gradient in their bulk without plasmas [114]. The effects of pH need to be further considered in future development of the model. For low power density operation for a period of less than 120 s, it is possible for atmospheric helium–oxygen plasmas to maintain the gas temperature at and near room temperature and to maintain the pH value of a downstream liquid sample with which the plasma is brought in contact [86, 113]. With much larger concentrations than other species, H_2O and O_2 have a fixed concentration with the H_2O concentration calculated at 300 K and O_2 at its saturated concentration in the water before plasma treatment. Boundary flux of O_3 is determined from Eq. (17) using Henry's coefficient of 29.58×10^{-2} [115, 116]. Initiation conditions of other species (at $t = 0$, $x \geq 0$) are given below

$$\begin{aligned} C_{H2O} &= 3.35 \times 10^{28} m^{-3};\ C_{O2} = 1.643 \times 10^{23} m^{-3} \\ C_{OH-} &= 6.02 \times 10^{19} m^{-3};\ C_{H+} = (6.02 \times 10^{19} + 5 \times 10^{11})\ m^{-3} \\ C_i &= 10^{11} m^{-3} \text{for other species than } H^+,\ OH^-,\ O_2 \text{and } H_2O \end{aligned} \quad (18)$$

The H^+ concentration is little higher than the OH^- concentration in order to retain the electrical neutrality in the liquid with the presence of other negative ions (e.g. O^-, O_2^-, O_3^-) and electrons. Plasma species other than H^+ and OH^- are likely to be involved in rapid chemical reactions in the gas–liquid boundary region, and therefore their concentrations are dynamically evolving. Their mass transfer is achieved by using their fluxes (see column 7–8 of "Appendix 1") and using the penetration model of Eq. (1) and (2). These are also illustrated in Fig. 3.

Plasma-Tissue Interaction Model

Intact human tissues including skin are known to present a considerable barrier to the penetration of drugs and antibiotics, and modern drug delivery technologies often recourse to minimal invasive strategies such as micro-needle arrays [30]. The challenge for effective delivery of reactive plasma species is similar, and this has encouraged the utility of microscopic gaseous channels created either naturally by a narrow wound trench into skin or artificially introduced as a delivery aid [31, 32]. Transport and on-site chemical reactions of plasma species through such channels are studied for both static and healing wounds [31, 32, 117], however thermal deposition from either heat transfer from the plasma generation region or from a flowing discharge current has yet to be analyzed theoretically for plasma-tissue interactions. Experimentally, thermal impact of plasmas on living tissues has been studied using plant, animal and human tissues [9, 10, 118–123]. For example, a recent pilot clinical trial for risk assessment of an atmospheric pressure plasma jet [123, 124] found that thermal damages were tolerable under its experimental conditions. Generalization of the conclusion must be cautious however, partly because the discharge current into the skin, the plasma treatment duration, and the skin surface condition interact closely and their complex interaction often prevents an informed use of their interdependence. More importantly, other factors may be at play, for example dielectric properties of living tissues vary with frequency thus strongly influencing thermal deposition in tissue and a strong electric field leads to sensitive nerve response and transmembrane protein denaturation. Thermal deposition and electric current passage in living tissues are distinct of gas plasma from conventional drugs including DNAs. These are important to be captured in an analysis framework of plasma-tissue interactions and in its use to unravel tissue-level functions, for example electrical and thermal injuries and plasma-based hyperthermia [38, 126].

Without the involvement of gas plasmas, human tissues exhibit large permittivity and small electrical conductivity at low frequencies (e.g. 50/60 Hz), but above radio frequencies (over 1 MHz) their permittivity reduces and their conductivity increases by many orders of magnitude from the values at 50/60 Hz, suggesting a strongly frequency-dependent Joule heating [125]. In addition, the passage of electric current through tissues lead to dielectric heating due to energy loss from oscillating dipoles of water molecules and dielectric heating increases with frequency. Furthermore, contact heating may be introduced on the skin surface. Depending on the thermal dose, Joule, dielectric and contact heating can cause damages through three different mechanisms. With little molecular level modeling and with direct experimental validation, macroscopic heat

transfer models have been shown to reliably describe all three thermal injury mechanisms of electricity [35, 127, 128], and are therefore used for our study. Less known is however nonthermal injury of electricity (or more specifically of electric field) [125, 129–131], for example degradation to transmembrane proteins and damage to phospholipid bilayer structure via irreversible electroporation. These are at present simulated largely with molecular dynamics and other microscopic models [132–136], yet how changes in molecular conformation at a sub-cellular level may be translated into changes to experimentally detectable tissue functions (e.g. non-thermal tissue injuries) remains elusive. From the success of modeling thermal injuries of electricity, it is logical to attempt an integration of the macroscopic models of thermal injuries of electricity with the molecular models of its nonthermal injuries. The key challenge here is an effective translation of nanometer variations in protein and lipid structures to tissue functions, particularly given that molecular modeling of proteins and protein structures are itself very challenging with prohibitive computational resources demand and are constantly developing [137–139].

For the ambient pressure plasmas considered here, the excitation frequency is at 13.56 MHz (see discussion below) at which the gas breakdown voltage is only a few hundreds volts. As shown in Fig. 4, the resulting voltage applied to a skin tissue of about 23 mm is no more than 22 V leading to a global electric field of <1 V/mm, much lower than the threshold electric field for electroporation. Not withstanding the possibility of low-level nonthermal electrical injury and its potentiation for thermal injuries, we consider in our model two common thresholds for thermal injury of electricity, namely a threshold temperature of 43 °C at the epidermis-dermis interface [35, 128] and a threshold for a dimensionless thermal injury index Ω described by the following heat damage equation [35, 128, 140, 141]:

$$\Omega = \int_0^t A \exp(-E_a/RT_n)dt \tag{19}$$

where E_a is the activation energy, R is the general gas constant, T_n is the temperature at a point in tissue, and A is a frequency factor that depends on molecular structure. The 43 °C threshold reflects the fact that temperature sensors of the skin tissue are not on the skin surface and that significant nerve stimulation takes place to induce a sensation of pain when the temperature at the epidermis-dermis interface is close to and above 43 °C [35]. Though deduced not from physics, this threshold is obtained from extensive experimental studies of inflammation and pain over many decades [35, 130, 131] and as such should not be regarded as a mere empirical indicator. On the other hand, Eq. (19) is based on a theory of Henriques and Moritz [142] that thermal damage to the skin structure (despite of the variation of different types of electrical injuries [131]) may be modeled by a chemical reaction process depending on the duration of the thermal burden, the rate of protein denaturation and the absolute temperature, and that this process is described with an Arrhenius model. The concept of Ω is used to reflect the extent of damage, for example he concept of identifies when cells start to suffer irreversible damage with a cell death probability of 63 % at a spatial location and Ω is related to a cell death probability of 99 % [35, 128, 140, 141, 143]. For the study presented here $E_a/R = 75{,}000$ K and $A = 31. \times 10^{98}$ s^{-1} using data in [35]. As the temperature is calculated for every point within a tissue bulk, an epidermis-dermis boundary temperature of 43 °C and Ω are used respectively in our model as the threshold for thermally induced pain and cellular damages.

When an ambient pressure gas plasma is placed in direct contact with human skin, thermal deposition in the plasma gives rise to contact heating as well as Joule and dielectric

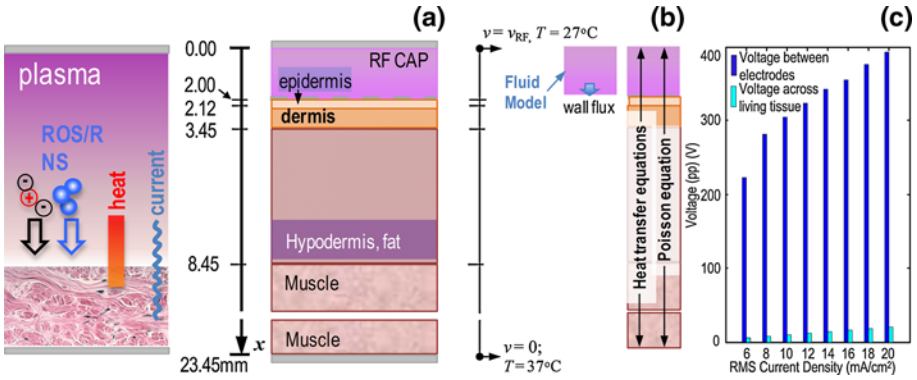

Fig. 4 **a** Plasma-tissue interaction with the plasma modeled using a fluid model and the tissue using an intact skin having its epidermis, dermis, hypodermis and muscle layers (a *white gap* is inserted in the muscle section to bring in the large muscle section into scale). The tissue thickness is 21.45 mm, and the plasma is sustained in a 2 mm He–N_2 gap and at 13.56 MHz; **b** the electrode away from the tissue ($x = 2$ mm) is connected to high voltage and kept at 27 °C, and at the end of the muscle section ($x = 23.45$ mm) the electrical potential is zero and the temperature is at the body temperature of 37 °C. Plasma dynamics and chemistry are modeled for the plasma region only, and heat transfer and electric field and current penetration are modeled throughout; **c** the electrical potential on the tissue surface is very close to zero as the vast majority of the external voltage is applied across the gas gap

heating through heat transfer into the tissue bulk. When the tissue-facing electrode is not grounded or the tissue is used as a floating electrode, the electric field is allowed to penetrate into the tissue thus making it possible to cause both thermal and nonthermal damages. A trade-off must be had between maximizing plasma-induced benefits and minimizing electrical and thermal damages. The complexity of how different factors may interact to influence a possible optimization necessitates a theoretical framework of analysis, and this may be illustrated in the example of frequency dependence. With a monotonic decrease with frequency of their permittivity and resistivity, human tissues have progressively reduced electrical insulation. This is desirable when within the safety range since lowered electrical insulation allows easy access to targets in cells and tissues, but not so if lowered electrical insulation results in compromised electrical safety. When properties of the gas plasma are factored into the optimization, high frequency operation is favored for stability of ambient pressure plasmas yet it also leads to lower breakdown voltage and so higher discharge current density (also larger gas heating) at a given dissipated power density [144–146].

Here we consider, as a starting point, radio-frequency atmospheric pressure plasma in a helium-nitrogen gap of 2 mm (N_2/He = 0.5 %) and at 13.56 MHz with the frequency effects left for a future report. The plasma is placed such that its tissue-facing electrode is in direct contact with an intact skin tissue with its layered structure as shown in Fig. 4a. The electrode away from the tissue is set at high voltage and at room temperature of 27 °C, and the tissue-facing electrode is allowed to float in its electrical potential and temperature. The ground is set at the end of the muscle section at $x = 23.45$ mm, where the temperature is set at the body temperature of 37 °C. As the tissue-facing electrode is of at least 37 °C, plasma generated dissipates less effectively to the surrounding area than the case of plasma-biofilm interactions. In other words, the gas temperature is higher in Fig. 4 than Fig. 3 for a given dissipated power density. Plasma dynamics and chemistry is modeled for the plasma region only using the same fluid treatment used for the biofilm study and

detailed in literature [63], whereas heat transfer and electric field are simulated for both the plasma and the skin tissue regions, as illustrated in Fig. 4b. As the tissue-facing electrode is allowed to float, it is important to estimate its electrical potential and broadly ensure electrical safety. Simulation data suggests that the effective impedance of the ionized gas gap is much larger than that of the tissue, resulting in the vast majority of the external voltage (95–97 %) to be applied over the gas gap and the electrical potential on the tissue-facing electrode is at most 22 V (see Fig. 4c). Therefore nonthermal injuries due to irreversible electroporation are very small, if any, and the electrode connection of Fig. 4a is safe. In the context electricity safety, electric current flowing into the tissue needs to be assessed. Health Canada has guidelines for the maximum electric current human can withstand for different exposure time in the frequency range of 0.1–110 MHz [152] and is shown in "Appendix 4". This is the additional safety threshold to the pain and protein denaturation thresholds, all of which are used in our model to translate the results of the heat transfer and electrical penetration modeling into thermal and electrical tolerance.

Our model considers intact skin tissue and leaves penetration of plasma species into the tissue bulk via gas channels to future studies. As an approximation, plasma fluxes are allowed to pass through the tissue-facing electrode without loss and onto the skin surface. The plasma model considers 7 species namely e, He^+, He_2^+, N_2^+, N_4^+, He^*, and He_2^*) and 19 chemical reactions among them identical to those in [147]. For easy illustration of their link to the governing equations of the tissue section, we list below the governing equations of the fluid model as follows:

$$\frac{\partial n_i}{\partial t} + \nabla\cdot\vec{\Gamma}_i = S_i \tag{20}$$

$$\frac{\partial n_e T_e}{\partial t} + \frac{5}{3}\nabla\cdot(T_e\vec{\Gamma}_e - n_e D_e \nabla T_e) = -e\vec{\Gamma}_e\cdot\vec{E} - \sum_j R_j\cdot E_j - 3\sum_i \frac{m_e}{m_i} k_B k_{el} n_e n_i (T_e - T) \tag{21}$$

$$\nabla\cdot\vec{E} = -\sum_i e n_i/\varepsilon_0 \tag{22}$$

$$\rho_g c_g \frac{\partial T}{\partial t} + \nabla\cdot(-k\nabla T) = Q \tag{23}$$

where n_e, T_e and D_e are respectively the density, the temperature and the diffusion coefficient of electrons; n_i, Γ_i, S_i are respectively the density of species i, its flux, and the rate of its generation and loss; ε_0 and T are the free space permittivity and the gas temperature; ρ_g, c_g and k are the density, the specific heat capacity and thermal conductivity of the gas; E is the electric field; and R_l and ΔE_j are the rate of the inelastic collisions and the energy loss due to inelastic collisions. Heavy particles are assumed to be at the gas temperature. The flux of species i is given by

$$\vec{\Gamma}_i = \text{sign}(q_i) n_i \mu_i \vec{E} - D_i \nabla n_i \tag{24}$$

Here q_i is the charge of species i and D_i, μ_i are respectively its diffusion and mobility coefficient. Q is the heating due to momentum transfer between electrons and species i and Joule heating of ions and given by [66]

$$Q = 3\sum_i \frac{m_e}{m_i} k_B k_{el} n_e n_i (T_e - T) + \vec{j_+}\cdot\vec{E} \tag{25}$$

where j_+, k_B are the ion current density and the Boltzmann constant; m_i and k_{el} are the mass of species i and its momentum transfer rate with electrons; and m_e is the mass of the electron.

The heat transfer into and through the tissue is described by Pennes' bio-heat transfer model of [127]

$$\rho_t c_t \frac{\partial T}{\partial t} = k\nabla^2 T + \varpi_b \rho_b c_b (T_b - T) + \sigma_s E^2 + q_{met} \tag{26}$$

where ρ_t, c_t, k and T are respectively the density, specific heat capacity, the thermal conductivity and the temperature of the tissue; ρ_t, c_b, ϖ_b and T_b are respectively the density, specific heat capacity, the perfusion rate, and temperature of the blood; q_{met} is heat generated due to metabolism, and σ_s is the electrical conductivity of tissue. Tissue temperature and gas temperature are solved together, so the symbol T is denoted to both. The second term on the right hand side represents the net heat due to blood perfusion, and the third is due to electrical heating. Equations (23) and (26) are of the same form, and can be solved continuously from the plasma region to the tissue region. Similarly the electrical potential is solved for both the plasma and tissue regions. At the boundary between the plasma and tissue, the boundary condition is

$$\varepsilon_p E_p - \varepsilon_s E_s = \sigma_e \tag{26}$$

with σ_d being the surface charge density on the plasma-tissue boundary and being equal to the time integral of the conduction current density flowing into the tissue, J_c. The conduction current density needs to satisfy

$$\frac{\partial n}{\partial t} + \nabla \cdot J_c = 0 \tag{27}$$

in the tissue region. Therefore Eqs. (20) and (21) are solved in the plasma region, eq.(27) is solved in the tissue region, and the heat transfer Eqs. (23) and (25) and Poisson's Eq. (22) are solved for both the plasma and the tissue regions. Thermal and dielectric parameters of the skin tissue and blood are listed in "Appendix 5" with source references [35, 148, 149]. It is worth mentioning for future model development that the integrated treatment of electrical and thermal phenomena in the plasma region and the tissue region has benefited from previous studies of electrical injuries, for example the coupling of the electrically induced heating mechanisms with Pennes' bio-heat transfer equation [149], capacitively coupled radio-frequency heating for hyperthermia of pelvis tumors [150], and similar studies of inductively coupled RF heating for hyperthermia [151].

Results and Discussions

The theoretical framework described in Section "Model Development" is developed by advancing biophysical models used in neighboring disciplines for integration with plasma physics and liquid-phase plasma chemistry models. With future development and improvement, it could be used to study a wide range of topics in plasma-biofilm and plasma-tissue interactions. Here as an example, we study plasma penetration into biofilms and onto intact skin tissues in order to establish the key limiting factors to plasma accessibility to a diseased region within a physical structure. In the former case, the focus is on transfer and penetration of physical matters (e.g. transient chemicals) into a porous

and hydrated structure. Here the key barrier to plasma access is likely due to the very significant reactivity of plasma chemistry due to rapid quenching of gaseous plasma species by water molecules. For most applications, the application of a plasma source is usually to treat a biofilm sample as a downstream load and as such little discharge current is fed to flow into the biofilm suggesting little or controlled electrical and heat transfer. In the case of intact skin tissues, the main barrier to plasma access is the dense tissue structure with few access entries (e.g. follicles of about 300 μm in diameter) that do not necessarily lead to the target area. The focus here is to look at the penetration of long-range fields specifically the electrical and thermal fields in the context of plasma tolerance and possible plasma-aided hyperthermia. Taken the two cases together, the case studies in this section cover mass and heat transfer as well as electromagnetic propagation in living tissues. It is worth mentioning the obvious desire to understand how plasma may be configured to reach a target buried deep inside a tissue and how the model developed here may be used to aid this objective. However this important challenge for the plasma technology should be left to future studies and reports once significant progress has been made.

Diffusion to a Downstream Gas Region

Diffusion of reactive plasma species into a downstream gas region provides a reference point to plasma penetration into a liquid and also provides information of recombination depth if a gas buffer is introduced between the plasma and a biological sample. Within the generation region of the He-O_2 plasma, Fig. 5 shows concentrations and wall fluxes of ground and excited state oxygen species and negative ions for O_2/He = 0–10 % as well as the pathway map of the key chemical reactions at O_2/He = 1 %. As shown in Fig. 5a, b, most reactive oxygen species have similar O_2/He dependences for both their concentrations. For bacteria in planktonic growth (i.e. not in a biofilm) and indeed biomolecules such as proteins on a slightly moist surface, atomic oxygen has long been considered as a key plasma oxidant [48, 153–157]. Another biologically important reactive oxygen species is the singlet delta oxygen molecule [158–161], and its concentration and wall flux are shown in Fig. 5a and b to have similar O_2/He dependence. For both atomic and single delta oxygen, their concentrations and wall fluxes are seen to peak in the narrow range of 0.5–1.0 %. At O_2/He = 1 %, Fig. 5c shows that their production is dominated by electron impact reactions, suggesting a clear optimization route by enhancing electron production. One exception to the similar O_2/He ratio dependences in species concentrations and wall fluxes is negative ions of oxygen molecules O_2^- or superoxide as known in biology [164, 165]. After reaching its peak around O_2/He = 0.8 %, the O_2^- concentration decreases monotonically with increasing O_2/He ratio. By contrast, the O_2^- wall flux increases monotonically with O_2/He. This contrast is due to the very short excursion distance of O_2^- at only 3–4 μm during the lifetime [63, 166], suggesting that O_2^- produced in the plasma bulk may not be able to reach the electrode and hence contribute to the wall flux. In general, O_2^- production is mainly through charge transfer of O_3^- via O and the larger O_3 concentration (hence O_3^- concentration) help increase the wall flux of O_2^- at large O_2/He ratios. Therefore the main optimization route for delivering O_2^- to a biological sample is through O_3^- different from those for O, O^* and O_2^*. This is perhaps more important for plasma treatment of mammalian cells, for which induction of cellular functions, for example through signaling pathways, is more important than in the case of bacterial inactivation.

Wall fluxes of neutral ROS of Fig. 5b (at O_2/He = 1 %) are allowed to diffuse through an exit electrode without loss into a downstream helium–oxygen ambience. Figure 6a

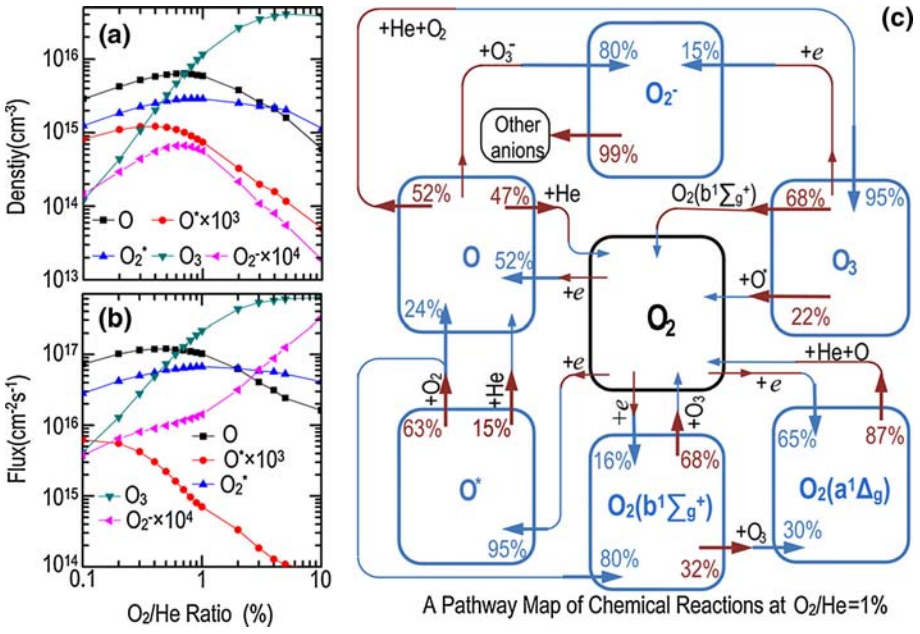

Fig. 5 Plasma chemistry in the generation region of an atmospheric pressure helium–oxygen plasma with the O_2/He ratio dependence of **a** the concentrations of its reactive oxygen species and **b** the wall flux of ROS for O_2/He = 0–10 %. Similar O2/He ratio dependences of concentrations and wall fluxes hold for most ROS apart from negative oxygen ions (or superoxide). At O_2/He = 1 %, the ROS pathway map of key generation and loss reactions is shown in **c**. For ground and excited state oxygen atoms as well as singlet delta oxygen, their production is through a similar pathway of electron impact reaction whereas the generation of superoxide is through charge transfer from O_3^-. In (c), *blue* and *red arrows* represent respectively generation and loss pathways and the percentage numbers associated are the percentage of a given pathway in the generation or the loss of the relevant ROS. *Larger* and *thicker arrows* indicate the dominant pathways each with a percentage value, and *small* and *thin arrows* indicate pathways of smaller contributions. For simplicity, pathways of less importance than shown are omitted (Color figure online)

shows the distance dependence, largely independent of the plasma-on time (10 s or 60 s) apart from O_3 for $x > 1$ cm. Using a threshold concentration of 10^{10}cm^{-3}, the penetration depth of excited state oxygen atoms is the shortest around 2 μm and that of $O_2(b^1\sum_g^+)$ is the second shortest of around 20 μm. The singlet delta oxygen and the ground state atomic oxygen have a similar penetration depth of 1 and 0.9 cm, respectively. O_2^- is not shown due to its low concentration (at least 4 orders of magnitude lower than others). Figure 6b suggests that at $x = 1$ mm downstream from the exit electrode O_3 molecules are produced mostly by $O + O_2 + He \rightarrow O_3 + He$ and lost to diffusion (40 %) and to dissociation (60 %). Singlet delta oxygen molecules are produced via diffusion of upstream singlet delta oxygen molecules, and are lost to dissociation. A different upstream O_2/He ratio (within the plasma generation region) would of course change the boundary concentrations of ROS, but the extent of change to their penetration depth is likely to be much smaller. Figure 6a shows that at $x = 100$ nm the O* and $O_2(b^1\sum_g^+)$ concentrations already show a downwards slope, indicating that their lifetimes are likely to be shorter than other neutral ROS and such characters have some but not dominant impact on their penetration distance.

Results of Fig. 6 suggest that the major neutral ROS beyond a few millimeters downstream from a helium–oxygen plasma region are the ground state atomic oxygen, the

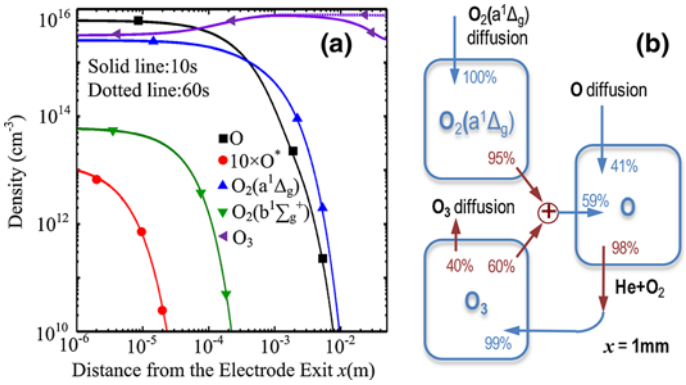

Fig. 6 Downstream gas-phase plasma chemistry at an upstream O_2/He = 1 % and with **a** ROS concentrations as a function of the distance from the exiting electrode at $t = 10$ s (*solid curve*) and $t = 60$ s (*dotted curve*); **b** the pathway map of key chemical reactions. *Blue* and *blue arrows* are used to indicate respectively the dominant reactions of generation and loss pathways, and a percentage value is given to each pathway to indicate the contribution in percentage term to the generation or loss of a given chemical species, in the same way as in Fig. 5 (Color figure online)

singlet delta oxygen, and the ozone. Since the plasma-sample distance is typically around 1 cm, their synergic interaction is likely to be at play on a (mostly dry) microbial sample. For most application scenarios where the sample is more than 1 mm away from the plasma generation region, the synergy appears to be associated with a reaction chain involving ground state atomic oxygen, singlet delta oxygen and ozone. For future reference, this is referred to as the O-O_2(a)-O_3 cycle chain. The data of Fig. 6 support the current view of oxygen atoms and singlet delta oxygen being important for microbial inactivation. It is worth mentioning that previous analyses and discussions of the identity of possible dominant ROS are often based on ROS concentrations in the plasma-generation region rather than at the downstream sample, and that little consideration has been given to how the lifespans of ROS may impact on their penetration depth into a downstream ambience. Figure 6 also shows a cliff of rapid concentration reduction of O and $O_2(a^1\Delta_g)$. This illustrates the possibility of a large variation in biological effects when the sample-plasma distance is slightly moved, for example a small move of 1 mm in the sample location between 2 and 10 mm could see a O concentration change of more than half order of magnitude. Even without other differences, a concentration cliff such as that for O and $O_2(a^1\Delta_g)$ between 1 and 10 mm could introduce large variation in experimental results from seemly identical experiments performed at different labs. At a distance much further than 1 cm away from the plasma-generation region, the dominant ROS is ozone and the chemical synergy ceases to be important. The above discussions offer previously little known observations that are distinctively different from the knowledge of plasma chemistry within the plasma region, and these are (1) downstream plasma chemistry involves progressively less and less plasma species; (2) for a practically meaningful plasma-sample distance of 1–10 mm, plasma chemistry is dominated by a O-O_2(a)-O_3 synergy; (3) the contribution of O and O_2(a) may change significantly with a small variation in the plasma-sample distance around 10 mm due to their concentration cliff of reduction; (4) for a plasma-sample distance much greater than 10 mm, the helium–oxygen plasma essentially become an ozone generator. These are likely to be useful for future plasma medicine experiments

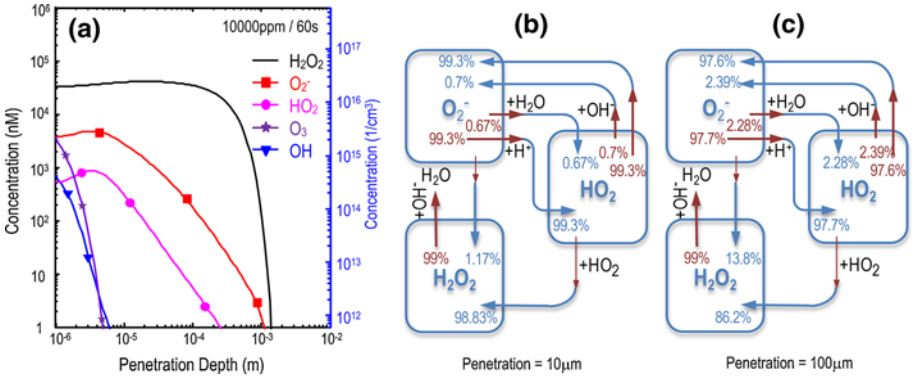

Fig. 7 **a** Dependence of ROS concentrations on the distance penetrating into a liquid bulk from the exiting electrode after 60 s and for an upstream O_2/He = 1 %. Liquid-phase reactions generate hydrogen-containing reactive species including H_2O_2, OH and HO_2 thus increasing the complexity of plasma chemistry but with a much reduced penetration depth down to <1.5 mm. The pathway chain map for key ROS is shown in **b** 10 mm and **c** 100 mm into the liquid. Identical to Fig. 5, *blue* and *blue arrows* are used to indicate respectively the dominant reactions of generation and loss pathways, and a percentage value is given to each pathway to indicate the contribution in percentage term to the generation or loss of a given chemical species (Color figure online)

Diffusion into Liquid Bulk

When a downstream liquid bulk replaces the downstream gas region of Section "Diffusion to a Downstream Gas Region", the incoming gaseous plasma species undergo diffusion as well as reactions with water molecules. Hydrogen-containing species are generated, including the generation of H^+ near the liquid surface through dehydration of ionic water clusters and the in-liquid generation of OH, OH^-, HO_2, HO_3, and H_2O_2. The concentration profile of plasma species from the gas phase and hydrogen-containing species into the bulk of the liquid layer is shown in Fig. 7a. Data below 1 μm are not shown, due to the gas–liquid boundary layer being of a micrometer scale and the uncertainties of detailed chemistry in the micrometer boundary layer.

Our numerical results suggest that the most unstable plasma species in the liquid are atomic oxygen and singlet delta oxygen with their penetration distance much <1 μm, and therefore they are unlikely to be involved in the inactivation of microbes embedded in a biofilm given the diameter of a single microbe being 0.2–2.0 μm. This is distinctly different from the gas phase where O and $O_2(a^1\Delta_g)$ are important for inactivation of largely dry microbes and biomolecules (see Fig. 6). After entering the liquid, O and $O_2(a^1\Delta_g)$ become converted into other reactive species within 1 μm and these other reactive species (e.g. O_2^-, H_2O_2, HO_2, OH, and O_3) become key antimicrobial agents in the liquid. This short penetration depth of O atoms identified by the diffusion–reaction model here is also reported by recent molecular dynamics simulations [162, 163]. Ozone concentration reduces when entering the liquid to satisfy Henry's law, but increases after a few micrometers into the liquid via quenching of O ($O + O_2 \rightarrow O_3$) and charge transfer of O_3^- ($OH + O_3^- \rightarrow O_3 + OH^-$). However plasma-induced species such as electron, H, OH, H_2O_2, O^- and O_2^-, introduce an array of O_3 loss pathways (see reaction no. 35, 46, 56, 63, 69, 76 and 84 in "Appendix 2") that are absent in the hydrogenation of pure ozone. Therefore the O_3 lifetime in liquid is much shorter with than without plasma. In the case of

OH radicals, their reactivity is very high and their lifetime in liquid is known to be on a nanosecond scale [167]. Therefore it is of little use to attempt an upstream generation of OH radicals in a vapor-containing plasma for downstream delivery into a liquid, and Fig. 7a indicates that this is also unnecessary because they are generated and sustained in the liquid phase via electrons, H^+, O^-, O_3^-, O_3, HO_3, H_2O_2 (see reaction no. 18, 20, 26, 78, 79, 82 and 84 in "Appendix 2"). Using 1 nM as a threshold concentration, the penetration depths of O_3 and OH radicals are both around 5–6 μm whereas the longer-living species of HO_2, O_2^- and H_2O_2 have a penetration depth of 0.25, 1.0, and 1.3 mm respectively. Figure 7b and 7c show the pathway chain map of plasma-induced liquid-phase chemistry at 10 and 100 μm beneath the liquid surface. Similar to that in the downstream gas ambience, there is a reaction cycle chain but among O_2^-, HO_2, and H_2O_2. While the biological relevance of O_2^- and H_2O_2 are well known [164, 165, 168, 169], hydroperoxyl (HO_2) is also a biologically important oxidant and may be involved in lipid peroxidation [170, 171]. It is involved with the production and loss of superoxide via $O_2^- + H_2O \Leftrightarrow HO_2 + OH^-$, but is a more powerful oxidant and reductant than O_2^- [171]. These discussions suggest that reactive oxygen species surviving more than 10 μm into a liquid bulk (or a highly hydrated biofilm) in Fig. 7 are known to be biological important and relevant.

In section "Gas–Liquid Boundary Region" and "Boundary Condition", the gas–liquid boundary is discussed to possess the rapid reaction chemistry on a sub-micrometer scale and as a result the fluxes of most gaseous plasma species are assumed to maintain their value. This assumption is also applied to the flux of hydrogen ions as that of O_2^+ due to the rapid charge transfer between their water clusters [see (9)]. Given the experimental difficulty of measuring H^+ concentration in a very thin boundary layer with active chemical reactions, we examine the sensitivity of our conclusion of a liquid-phase reaction cycle of O_2^-, HO_2, and H_2O_2 by increasing and decreasing the proton flux at the gas–liquid boundary by a factor of 10. To maintain electrical neutrality, adjustment to fluxes and concentrations of ionic species at the gas–liquid boundary is made. The results are shown in Fig. 8, showing broadly similar penetration profiles with O_2^- and H_2O_2 being the reactive oxygen species surviving beyond 10 μm. When the proton flux is increased by ten times of its value in Fig. 7 ($\Gamma_{H+,0} = 8.9 \times 10^{15}$ m^{-2} s^{-1}), or $\Gamma_{H+} = 10\Gamma_{H+,0}$, Fig. 8b show that the HO_2 concentration becomes lower than OH and O_3 concentrations and that the HO_2 penetration distance also becomes shorter. This change from Fig. 7a is largely due to the change in the boundary conditions. Therefore the overall picture is that (1) the most dominant species are O_2^- and H_2O_2 regardless the ROS fluxes entering into the liquid; (2) HO_2 plays a role of the third most significant ROS for $\Gamma_{H+} \leq \Gamma_{H+,0} = 8.9 \times 10^{15}$ m^{-2} s^{-1}; (3) the concentration levels of O_2^- and H_2O_2 are sensitively dependent on their boundary concentrations at the liquid surface.

The results of spatial profiles of liquid-phase reactive plasma species in Figs. 7 and 8 may be related to cell functions at a population level (i.e. not individual cells). In the context of biofilm inactivation, most biofilms have a thickness in the range of 10–350 μm [172–175] and therefore the penetration depth of O_2^- and H_2O_2 beyond 10 μm and up to 1 mm looks promising provided their concentrations are adequate for inactivating bacteria. Plasma penetration into a biofilm is not well studied, but data reported so far in literature suggest that atmospheric He + O_2 plasma can reach 10–15 μm into *Pantoea agglomerans* biofilm [176] and 15 μm into *Porphyromonas gingivalis* biofilm after 60–120 s [177]. For planktonic bacteria, the minimum inhibition concentration (MIC) of hydrogen peroxide is 1 mM against *E. coli* [178] and 50 mM against *S. aureus* [179] whereas that of O_3 is 4 μM against vegetative cells [180]. At a penetration depth of 10 μm and for $\Gamma_{H+} = 0.1\Gamma_{H+,0}$,

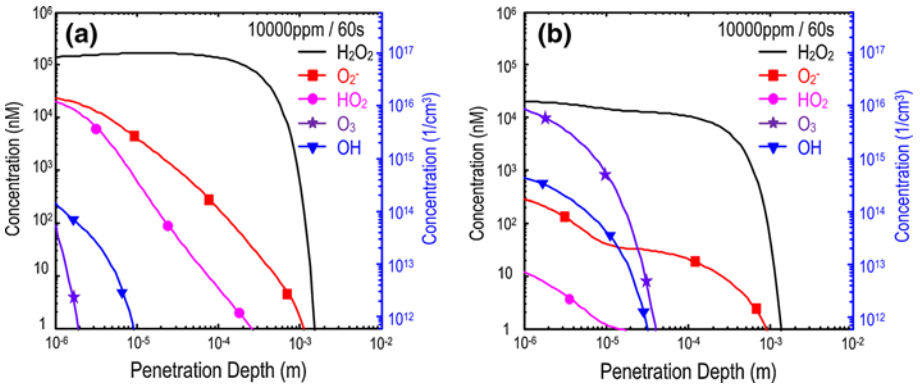

Fig. 8 Penetration of reactive oxygen species into a liquid bulk under the same condition as that in Fig. 7 apart from the proton flux at the liquid surface Γ_{H+} changed from its nominal value of $\Gamma_{H+,0} = 8.9 \times 10^{15}$ m^{-2} s^{-1} for Fig. 7 in **a** $\Gamma_{H+} = 0.1\Gamma_{H+,0}$; and **b** $\Gamma_{H+} = 10\Gamma_{H+,0}$. Concentrations of other ionic species at the gas–liquid boundary are adjusted to maintain electrical neutrality

Γ_{H+0} and $10\Gamma_{H+,0}$, the O_3 concentration is « 1nM, « 1nM, 0.9 μM respectively whereas the H_2O_2 concentration is 0.2, 0.04 and 0.02 mM respectively. These are at least one order of magnitude below the individual MIC for O_3 and H_2O_2. The experimental evidence of effective biofilm inactivation to 10–15 μm with atmospheric helium–oxygen plasmas suggest the existence of mutual potentiation of surviving ROS such as O_3, H_2O_2 and O_2^-, and in the case of $\Gamma_{H+} = 10\Gamma_{H+,0}$ (Fig. 8b) possible potentiation of the antimicrobial capacity of O_3, H_2O_2 and O_2^- by OH. Given the possible mutual potentiation, it is plausible that the synergistic combination of liquid-phase plasma species leads to an equivalent single-specie concentration (either O_3 or H_2O_2) of at least one order of magnitude higher than that in Figs. 7a and 8 and hence above the MIC for vegetative cells. Therefore the penetration data of ROS and their concentration are reasonably consistent with experimental observations of biofilm inactivation [176, 177]. Enhancement of ROS concentration on the liquid surface and manipulation of liquid phase chemistry such as that in Fig. 7b should lead to greater penetration, as indicated in a recent study of reaching 25.5 μm into *E. faecalis* biofilm using an air plasma [181].

The above direct comparison of liquid-phase plasma simulation results in Fig. 7 and 8 with experimental data of plasma biofilm inactivation is very encouraging with a first demonstration of the feasibility of how liquid plasma chemistry at a molecular level may be used to quantitatively interpret biological phenomena at a cell population level. This is helped by considerable reduction of the complexity of gas-phase chemistry when delivered into liquid, despite of difficulties in dealing with the mass transfer across the gas–liquid boundary and the uncertainty over some reaction and transport parameters. At present, the plasma-biofilm model of Fig. 3 does not consider additional support to mass transfer by a moderate thermal gradient from the plasma region to the biofilm, the acidification of the liquid by nitrogen species, and the enhanced bactericidal capacity by synergizing bactericidal plasma species with moderately acidified liquid [182]. The current plasma-biofilm model does consider change to pH due to H^+ and finds the change to pH is very small under conditions studied here. With an optimization of plasma chemistry, heat-assisted mass transfer, and liquid acidification, we expect to extend the plasma penetration into biofilms to 40–50 μm. This would make CAPs as a

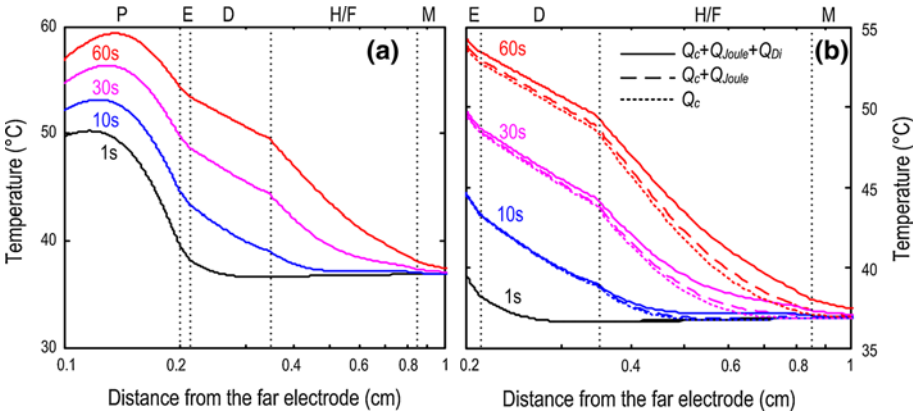

Fig. 9 Spatial profiles of the gas and tissue temperature in the plasma (P), epidermis (E), dermis (D), hypodermis/fat (H/F) and muscle regions at different plasma-on time from 1 to 60 s for a constant discharge current density of 10 mA/cm^2. Temperature profile shows in **a** the generated heat is primarily deposited in the gas region and very little is deposited in the muscle region (shown only to $x = 1$ cm, the total simulation space is to $x = 2.345$ cm); **b** the heating is predominantly caused by contact heating with Joule and dielectric heating accounting for at most 2 °C. A plasma-on time of <30 s is sufficient to trigger a sensation of pain at 10 mA/cm^2, consistent with experimental observations

viable option against many biofilms. The model of Fig. 3 may now be used to aid future biofilm inactivation experiments.

Thermal and Electrical Penetration into Skin

Gas and tissue temperatures are numerically obtained using the plasma-tissue interaction model of Fig. 4 and are shown in Fig. 9 for the plasma and the skin regions (including epidermis, dermis, hypodermis and fat, and muscle) at a discharge current density of 10 mA/cm^2. Figure 9a shows that the majority of heat deposition (hence temperature rise) is in the gas region and very little is delivered deep into the muscle region, the latter of which is similar to the case of radio frequency heating without the involvement of gas plasma. While not directly studied, heating of the muscle region is likely to be achieved at frequencies in and above the microwave band without or with gas plasmas. It is also shown that the temperature rise in the epidermis and dermis is quick with the temperature at the epidermis/dermis interface $T_{e/d}$ increasing to more than 43 °C after a plasma-on time of <30 s. Figure 9b shows that contact heating dominates whereas Joule and dielectric heating start to contribute after 10 s. The most significant effect of the Joule and dielectric heating is to induce heating deeper into the skin tissue than the contact heating, and this is through the absorption of electromagnetic energy by polarized molecules and macro-molecules such as water and fat.

It is possible to introduce mechanical and other cooling mechanisms to reduce the skin surface temperature. This reduces the contribution of the contact heating and hence thermal injuries to the skin surface, in which case the contribution of the Joule and dielectric heating increases proportionally. For delivering a maximum amount reactive plasma species to a living tissue, this helps increase the current density and hence plasma dose without pushing $T_{e/d}$ above 43 °C. The extent of the Joule and dielectric heating is largely controlled by the frequency, and therefore may be mitigated by reducing the frequency and

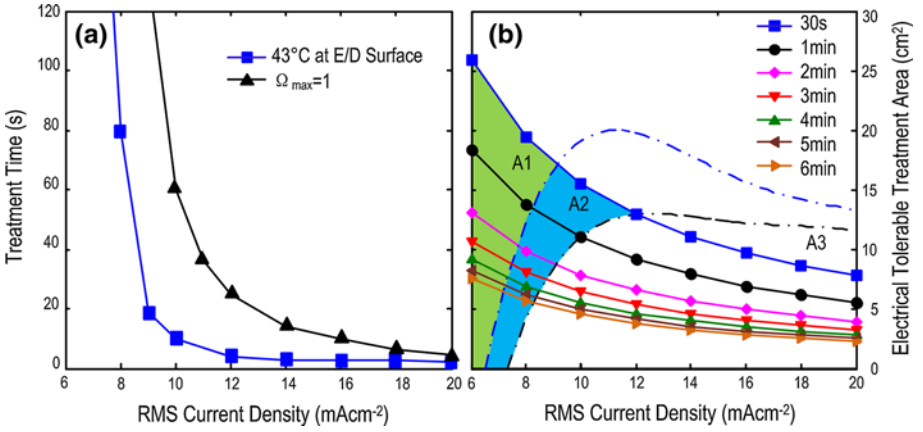

Fig. 10 Thermal and electrical safety map with **a** showing the thermal safety ceiling using a treatment time vs current density threshold for induction of skin pain and significant protein denaturation and cell death (~63 %) and **b** showing the electrical safety ceiling using the electric current limit Guideline of Health Canada [152] and the maximum permissible treatment area deduced from the threshold discharge current density in **a**. Regions A1, A2, and A3 include the thermal safety ceiling shown in **a** and they indicate respectively regions of safety (A1), sensation of pain (A2), and irreversible thermal injuries (A3). The electrically safe regions are those under the curves at different treatment times

so reducing the electromagnetic heating of polarized molecules. This technique needs to be assessed with the constrain of larger discharge current density of ambient pressure plasmas at a lower excitation frequency. An alternative is to use pulse modulated radio-frequency plasmas [183, 184] not because of the reduction to the gas-phase heating but because of the heat dissipation during the plasma-off phase. Again, detailed analysis needs to be performed as the pulse modulation is typically in the kilohertz range and the electric current safety is much more stringent than indicated in "Appendix 4".

In the context of hyperthermia, it is often of interest to induce heating deep into tissue and in practice this is often met with a considerable heating in the hypodermis and fat region [149, 150, 185] without plasma. Plasma-based hyperthermia is likely to be challenged similarly as Fig. 9b shows a greater contribution of Joule and dielectric heating in the fat region than the dermis region. The advantage of plasma-based hyperthermia is the control of tissue heating and electric field by dumping most heat and applied voltage in the gas region (hence is safer) and the benefits of reactive plasma species especially for open wounds albeit plasma ROS penetration needs to be studied.

The threshold for sensation of pain ($T_{E/D} < 43$ °C) and for irreversible thermal injuries [Eq. (19)] may be obtained by plotting the plasma-on time (or plasma treatment time) as a function of the discharge current density, as shown in Fig. 10a. The rapid reduction in the treatment time when the RMS current density is above 8 mA/cm^2 suggests an onset of rapid accumulation of heat in the skin tissue. For most atmospheric pressure helium–oxygen plasmas, the discharge current density is usually in a range of 5–100 mA/cm^2 in the kilohertz range and around or even above 1 A/cm^2 at and above radio frequencies. Such plasmas are always, and quite rightly so from the standpoint of plasma physics, known to nonthermal. Yet the prevailing interpretation of the word "nonthermal" in the context of electrical injuries is associated with a temperature some 6 °C above the body

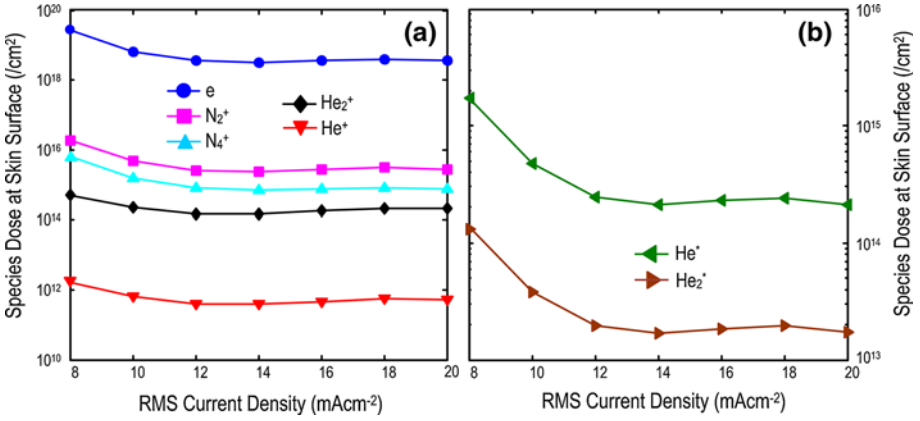

Fig. 11 Plasma dose measured as the product of the flux to the skin surface and the treatment time as a function of the RMS current density for **a** charged species and **b** neutral species. Here electrons and ionic nitrogen species as well as metastable helium species are used to represent the plasma dose and its dependence on the current density

temperature, highlighting the need to be clear and definitive in the different interpretations of the same word. It also highlights the need to review the measurement criteria for thermal tolerance of living tissues under plasma treatment.

Similarly important is the seemingly little appreciated fact that electrical current tolerance should not be extrapolated from the discharge current density but the current itself. This has a direct impact on the endeavors to scale up plasma jets and microplasmas for large area treatment of human tissues [186, 187]. It should be noted that the areas for safe treatment are <25 cm^2 at most, corresponding to a tissue area having a diameter <5.6 cm. For tissues with larger treatment area, innovative use of ambient pressure plasmas must be introduced including the reduction or removal of the discharge current that is allowed to flow into the tissue, for example using indirect plasma treatment of living tissues. The discussion here is relevant for radio frequencies (above 0.1 MHz), for which the voltage applied to the skin tissue is small and nonthermal injuries due to strong electrical fields are unlikely to be significant. It should be noted that at kilohertz frequencies the breakdown voltage of gas is larger and the electric field is more likely to be at the electroporation level [31, 32]. Nonthermal electrical injuries due to irreversible electroporation and electrocomformational protein denaturation are as a result more likely. Therefore the results discussed above for 13.56 MHz need to be reassessed. It is worth commenting that controlled and modest thermal injuries of electricity may become a necessary sacrifice in dealing with wounds and cancers when no alternative treatment is available. In this regard, it is useful to recall the discussion in Introduction that the electric field may interact with the mitochondrial membrane to produce ROS [36] and a penetrating electric field may induce an on-site ROS production inside the tissue.

Within the thermal and electrical safety as described in Fig. 10, the fluxes of plasma species onto the skin surface may be used to indicate the choices of the discharge current density. Using a form of the plasma dose, without generalization and without specific chemistry for a given application, as the product of the skin surface plasma flux and the plasma treatment time, Fig. 11 shows a very similar trend for all charged and neutral

species. Essentially a long treatment time outweighs the benefits of a large plasma flux achieved with a large current density, the latter of which is restricted by electrical and thermal tolerance. The results in Fig. 11 seem straightforward and simplistic, but are useful to highlight the need to bring in electrical and thermal safety considerations in designs of plasma-tissue interaction experiments, particularly if such experiments are intended for clinical trials. With future improvements (e.g. plasma chemistry in the presence of skin surface) and with other important factors included in future, the current plasma-tissue interaction model of Fig. 4 provides a framework for analysis of key interlinked and sometimes conflicting requirements in efficacy and safety of plasma induced biological effects.

For almost all biophysical and biochemical models, a central question has been how molecular level modeling is linked to a change in clinical functions that could be diagnosed. Similar to the observation drawn for the plasma-biofilm interaction model of Fig. 3, the plasma-tissue interaction model of Fig. 4 bridges a quantitative description of plasma physics to a tissue-level function (i.e. the electrical and thermal safety and plasma-based hyperthermia).

Concluding Remarks

This work reports the development, and the comparison with experimental data when available, of a model framework for plasma-biofilm and plasma-tissue interactions, both bridging the quantitative descriptions of physics and chemistry to experimentally detectable functions at either a cell population level (i.e. the biofilm) or a tissue level (i.e. the skin tissue). For plasma-biofilm interactions, a reactive penetration model is developed for mass transfer of highly transient plasma species across the gas–liquid boundary and a liquid bulk is used to model usually highly hydrated biofilm. Numerical prediction of plasma penetration using the plasma-biofilm interaction model is in good agreement with available experimental data of plasma inactivation of different biofilms. For plasma interactions with intact skin tissues, the model development brings in the knowledge of the neighboring field of electrical injuries, both thermal and nonthermal, by considering the onset for pain sensation and for considerable transmembrane protein denaturation as well as electric current threshold to human body as a panel of tolerance and safety thresholds. As a result, the plasma-tissue interaction provides a well-defined framework to assess electrical and thermal safety for CAP systems to be used directly on human and to identify ways to mitigate relevant risks whilst maximizing beneficial plasma effects. This model could also be used to explore the possibility and indeed improvement of plasma-based hyperthermia as well as of on-site production of ROS/RNS in tissues by a penetrating electric field.

The model framework has clear room for further improvement and development, for example the inclusion of reactive nitrogen species, the assisted mass transfer across the gas–liquid boundary by temperature and pressure gradients, the onset of liquid acidification and its synergy with bactericidal plasma species for biofilm inactivation, the inclusion of pore formation at the cell and (skin) tissue level, and of course the inclusion of relevant biophysical and chemical models from neighboring disciplines. This work is a beginning of the development of quantitative analysis tools for plasma biomedicine, and is hoped to help mitigate the variation and the lack of control in the conditions of plasma-biofilm and plasma-tissue interactions that once plagued the progress of plasma

biomedicine in 1950's. The work presented here should also be placed in the context of biophysical models and their common characters. Regardless specific subject areas or specific application contexts, biophysical models are powerful but rare if they have capability to predict population-level or tissue-level functions. Atomic or molecular level modeling is precise but often impossible to be extrapolated for prediction of cell or tissue functions, whereas phenomenological or partially phenomenological models can describe tissue functions under specific conditions but are inappropriate as a generic tool due to the lack of their underpinning science. The interaction models presented here appear to have been successful in bridging quantitative modeling of plasma chemistry and electrical heating of tissues to clear functions at a biofilm level or a tissue level. This is very encouraging. With future improvement, the plasma interaction models could become an indispensible component in an underpinning knowledge base with which derive and develop protocols and standards in plasma biomedicine.

As infectious biofilms and chronic wounds are significant societal challenges and also two major targets of plasma biomedicine, it is useful to summarize the findings that the plasma-biofilm and plasma-tissue interaction models have already unraveled. These are:

- Plasma penetration into biofilm—(1) the experimentally observed plasma penetration depth of 10–20 μm agrees with the penetration depth of plasma chemistry under typical conditions of low-power He + O_2 CAPs; (2) optimization through plasma chemistry, liquid acidification and heat and pressure assisted mass transfer could enhance the plasma penetration depth to 40–50 μm, offering an option against many biofilm inactivation (the biofilm thickness usually being 10–100 μm);
- Dry downstream chemistry (from the plasma region)—(1) the key reactive plasma species are O, O_2(a) and O_3 in the gas phase in a gaseous downstream region without nitrogen and their penetration depths (with a minimum concentration of 10 cm^{-3}) are respectively 0.9, 1.0 and well above 10 cm; (2) the O and O_2(a) concentrations undergo a cliff at x = 1 cm of rapid reduction of half order of magnitude for $\Delta x = 1$ mm, suggesting a source of variation in the inactivation efficacy; (3) the synergetic interplay among O, O_2(a) and O_3 diminishes after x = 1.5–2 cm downstream.
- Wet downstream chemistry (in biofilm)—(1) the key reactive plasma species are now O_2^-, H_2O_2 and HO_2 or O_2^-, H_2O_2 and O_3, a result of rapid liquid-phase reactions involving O and O_2(a); (2) the penetration depths of O_2^- and H_2O_2 with a minimum concentration of 1 nM are 1–1.2 mm with HO_2 in the range of 20–250 μm and O_3 of 5–40 μm. The low penetration depth of O_3 is due to additional loss mechanisms by charged particles; (3) O_2^- and H_2O_2 appear to be locked together and therefore their synergy is largely maintained. The liquid-phase plasma-induced chemistry shows similarity to chemistry of redox biology [188, 189] but also clear difference due to the presence of charged species.
- Electrical and thermal tolerance of living tissues to RF atmospheric plasmas—(1) the key risk of electrical injuries are thermal in nature with the contact heat being most significant and Joule and dielectric heating capable of delivering heat into the hypodermis region; (2) safety is largely influenced by the induction of pain sensation, protein denaturation and the lethal dose of the electric current; (3) long plasma treatment time at low discharge current density permits a larger plasma doses to the skin surface than short treatment time at high current density.
- RF plasma-based hyperthermia—offers a build-in safety mechanism of having the current density limited by the gas gap and therefore can be applied rapidly when compared to pure radio-frequency only hyperthermia.

The principle of the plasma-biofilm and plasma-tissue interaction models should remain the same when they are extended to ambient pressure plasmas in other gases, and the framework of the models also allow for improvements and other biophysical models to be brought in. In the case of plasma-biofilm interactions, the model could be modified for other applications of liquid-containing plasmas such as nanoparticle fabrication [190] and wastewater management [191]. The plasma-tissue interaction model on the other hand could be used for food and agriculture applications for example plasma treatment of crops, vegetable and fruits.

Acknowledgments This work was supported by the National Natural Science Foundation of China (Grant No. 51307134 and 51221005), and Old Dominion University, USA.

Appendix 1

See Table 1.

Table 1 Concentrations and fluxes at different transport nodes at O_2/He = 1 %

At the liquid-facing electrode			In the reactive gas film			Entering the liquid phase	
Species	C_i (cm^{-3})	Γ_i (m^{-2} s^{-1})	Species	C_i (cm^{-3})	Γ_i (m^{-2} s^{-1})	Species	Γ_i (m^{-2} s^{-1})
e	4.3×10^8	9.0×10^{15}	e	4.3×10^8	9.0×10^{15}	e	9.0×10^{15}
O^-	2.6×10^7	7.3×10^{11}	O^-	2.6×10^7	7.3×10^{11}	O^-	7.3×10^{11}
O_2^-	7.0×10^6	1.4×10^{11}	O_2^-	7.0×10^6	1.4×10^{11}	O_2^-	1.4×10^{11}
O_3^-	7.4×10^5	1.2×10^{10}	O_3^-	7.4×10^5	1.2×10^{10}	O_3^-	1.2×10^{10}
O_4^-	3.7×10^4	5.1×10^8	O_4^-	3.7×10^4	5.1×10^8	H^+	8.9×10^{15}
He^+	6.7×10^3	9.9×10^8	He^+	6.7×10^3	9.9×10^8	O	1.0×10^{17}
He_2^+	7.4×10^4	1.9×10^{10}	He_2^+	7.4×10^4	1.9×10^{10}	$O(^1D)$	6.3×10^{11}
O^+	1.2×10^8	2.9×10^{13}	O^+	1.2×10^8	2.9×10^{13}	$O(^1S)$	7.2×10^{10}
O_2^+	2.4×10^{10}	5.1×10^{15}	$H^+ \cdot (H_2O)_n$	4.8×10^{10}	8.9×10^{15}	$O_2(a^1\Delta_g)$	6.6×10^{16}
O_4^+	2.4×10^{10}	3.8×10^{15}	O	4.1×10^{14}	8.7×10^6	O_3	eq.(14)
He^*	8.4×10^4	4.2×10^9	$O(^1D)$	2.5×10^9	1.0×10^{17}	HO_2	produced in the liquid phase
He_2^*	2.5×10^2	8.7×10^6	$O(^1S)$	2.9×10^8	6.3×10^{11}	HO_3	
O	4.1×10^{14}	1.0×10^{17}	$O_2(a^1\Delta_g)$	3.8×10^{14}	7.2×10^{10}	H_2	
$O(^1D)$	2.5×10^9	6.3×10^{11}	$O_2(b^1\Sigma_g^+)$	5.2×10^{12}	6.6×10^{16}	OH	
$O(^1S)$	2.9×10^8	7.2×10^{10}	$O_2(v)$	2.4×10^{12}	9.2×10^{14}	OH^-	
$O_2(a^1\Delta_g)$	3.8×10^{14}	6.6×10^{16}	O_3	1.5×10^{15}	4.3×10^{14}	HO_2^-	
$O_2(b^1\Sigma_g^+)$	5.2×10^{12}	9.2×10^{14}					
$O_2(v)$	2.4×10^{12}	4.3×10^{14}					
O_3	1.5×10^{15}	2.2×10^{17}					

Appendix 2

See Table 2.

Table 2 Liquid phase chemical reactions

No	Chemical Reactions	Rates [s^{-1}or $M^{-1}s^{-1}$]	Ref
1	$O + O_2 \rightarrow O_3$	4.0×10^9	[79]
2	$O + O \rightarrow O_2$	2.8×10^{10}	[79]
3	$O_2a + H_2O \rightarrow O_2 + H_2O$	4.9×10^3	[80]
4	$O_2a + OH \rightarrow O_2 + OH$	2.2×10^3	[80]
5	$O(1d) + H_2O \rightarrow H_2O_2$	1.8×10^{10}	[81]
6	$O(1d) + H_2O \rightarrow 2OH$	2.3×10^{-10}	[82]
7	$H^+ + OH^- \rightarrow H_2O$	1.4×10^{11}	[78]
8	$H_2O \rightarrow H^+ + OH^-$	1.4×10^{-3}*	[77]
9	$H_2O_2 \rightarrow H^+ + HO_2^-$	$1.12 \times 10^{-1*}$	[77]
10	$H^+ + HO_2 \rightarrow H_2O_2$	5.0×10^{10}	[77]
11	$H_2O_2 + OH^- \rightarrow HO_2^- + H_2O$	1.3×10^{10}	[77]
12	$HO_2^- + H_2O \rightarrow H_2O_2 + OH^-$	5.8×10^7*	[77]
13	$e + H_2O \rightarrow H + OH^-$	1.9×10^1	
14	$H + OH^- \rightarrow e^- + H_2O$	2.2×10^7	[77]
15	$H \rightarrow e^- + H^+$	3.9*	[77]
16	$e + H^+ \rightarrow H$	2.3×10^{10}	[77]
17	$OH + OH \rightarrow O^- + H_2O$	1.3×10^{10}	[77]
18	$O^- + H_2O \rightarrow OH + OH^-$	1.03×10^8*	[77]
19	$OH \rightarrow O^- + H^+$	1.26×10^{-1}*	[77]
20	$O^- + H^+ \rightarrow OH$	1.0×10^{11}	[77]
21	$HO_2 \rightarrow O_2^- + H^+$	1.35×10^6*	[77]
22	$O_2^- + H^+ \rightarrow HO_2$	5.0×10^{10}	[77]
23	$HO_2 + OH^- \rightarrow O_2^- + H_2O$	5.0×10^{10}	[77]
24	$O_2^- + H_2O \rightarrow HO_2 + OH^-$	18.5767*	[77]
25	$e + OH \rightarrow OH^-$	3.0×10^{10}	[77]
26	$e + H_2O_2 \rightarrow OH + OH^-$	1.1×10^{10}	[77]
27	$e + O_2^- + H_2O \rightarrow HO_2^- + OH^-$	$1.3 \times 10^{10}/[H_2O]\ M^{-2}s^{-1}$	[77]
28	$e + HO_2 \rightarrow HO_2^-$	2.0×10^{10}	[77]
29	$e + O_2 \rightarrow O_2^-$	1.9×10^{10}	[78]
30	$2e + 2H_2O \rightarrow H_2 + 2OH^-$	$5.5 \times 10^9/[H_2O]^2\ M^{-3}s^{-1}$	[77]
31	$e + H + H_2O \rightarrow H_2 + OH^-$	$2.5 \times 10^{10}/[H_2O]\ M^{-2}s^{-1}$	[77]
32	$e + HO_2^- \rightarrow O^- + OH^-$	3.5×10^{10}	[77]
33	$e + O^- + H_2O \rightarrow OH^- + OH^-$	$2.2 \times 10^{10}/[H_2O]\ M^{-2}s^{-1}$	[77]
34	$e + O_3^- + H_2O \rightarrow O_2 + 2OH^-$	$1.6 \times 10^{10}/[H_2O]\ M^{-2}s^{-1}$	[77]
35	$e + O_3 \rightarrow O_3^-$	3.6×10^{10}	[77]
36	$H + H_2O \rightarrow H_2 + OH$	1.1×10^{10}	[77]
37	$H + O^- \rightarrow OH^-$	1.0×10^{10}	[77]
38	$H + HO_2^- \rightarrow OH + OH^-$	9.0×10^{10}	[77]
39	$H + O_3^- \rightarrow OH^- + O_2$	1.0×10^{10}	[77]
40	$H + H \rightarrow H_2$	7.8×10^9	[77]
41	$H + OH \rightarrow H_2O$	7.0×10^9	[77]
42	$H + H_2O_2 \rightarrow OH + H_2O$	9.0×10^7	[77]
43	$H + O_2 \rightarrow O_2$	2.1×10^{10}	[77]

Table 2 continued

No	Chemical Reactions	Rates [s^{-1}or $M^{-1}s^{-1}$]	Ref
44	$H + HO_2 \rightarrow H_2O_2$	1.8×10^{10}	[77]
45	$H + O_2^- \rightarrow HO_2^-$	1.8×10^{10}	[77]
46	$H + O_3 \rightarrow HO_3$	3.8×10^{10}	[77]
47	$2OH \rightarrow H_2O_2$	3.6×10^{9}	[77]
48	$OH + HO_2 \rightarrow H_2O + O_2$	6.0×10^{9}	[77]
49	$OH + O_2^- \rightarrow OH^- + O_2$	8.2×10^{9}	[77]
50	$OH + H_2 \rightarrow H + H_2O$	4.3×10^{7}	[77]
51	$OH + H_2O_2 \rightarrow HO_2 + H_2O$	2.7×10^{7}	[77]
52	$OH + O^- \rightarrow HO_2^-$	2.5×10^{10}	
53	$OH + HO_2^- \rightarrow HO_2 + OH^-$	7.5×10^{9}	[77]
54	$OH + O_3^- \rightarrow O_3 + OH^-$	2.6×10^{9}	[77]
55	$OH + O_3^- \rightarrow 2O_2^- + H^+$	6.0×10^{9}	[77]
56	$OH + O_3 \rightarrow HO_2 + O_2$	1.1×10^{8}	[77]
57	$HO_2 + O_2^- \rightarrow HO_2^- + O_2$	8.0×10^{7}	[77]
58	$HO_2 + HO_2 \rightarrow H_2O_2 + O_2$	7.0×10^{5}	[77]
59	$HO_2 + O^- \rightarrow O_2 + OH^-$	6.0×10^{9}	[77]
60	$HO_2 + H_2O_2 \rightarrow OH + O_2 + H_2O$	5.0×10^{-1}	[77]
61	$HO_2 + HO_2^- \rightarrow OH + O_2 + OH^-$	5.0×10^{-1}	[77]
62	$HO_2 + O_3^- \rightarrow 2O_2 + OH^-$	6.0×10^{9}	[77]
63	$HO_2 + O_3 \rightarrow HO_3 + O_2$	5.0×10^{8}	[77]
64	$2O_2^- + 2H_2O \rightarrow H_2O_2 + O_2 + 2OH^-$	$1.0 \times 10^{2}/[H_2O]^2$ $M^{-3}s^{-}$	
65	$O_2^- + O^- + H_2O \rightarrow O_2 + 2OH^-$	$6.0 \times 10^{8}/[H_2O]$ $M^{-2}s^{-1}$	[77]
66	$O_2^- + H_2O_2 \rightarrow OH + O_2 + OH^-$	1.3×10^{-1}	[77]
67	$O_2^- + HO_2^- \rightarrow O^- + O_2 + OH^-$	1.3×10^{-1}	[77]
68	$O_2^- + O_3^- + H_2O \rightarrow 2O_2 + 2OH^-$	$1.0 \times 10^{4}/[H_2O]$ $M^{-2}s^{-1}$	[77]
69	$O_2^- + O_3 \rightarrow O_3^- + O_2$	1.5×10^{9}	[77]
70	$2O^- + H_2O \rightarrow HO_2^- + OH^-$	$1.0 \times 10^{9}/[H_2O]$ $M^{-2}s^{-1}$	[77]
71	$O^- + O_2 \rightarrow O_3^-$	3.6×10^{9}	[77]
72	$O^- + H_2 \rightarrow H + OH^-$	8.0×10^{7}	[77]
73	$O^- + H_2O_2 \rightarrow O_2^- + H_2O$	5.0×10^{8}	[77]
74	$O^- + HO_2^- \rightarrow O_2^- + OH^-$	4.0×10^{8}	[77]
75	$O^- + O_3^- \rightarrow 2O_2^-$	7.0×10^{8}	[77]
76	$O^- + O_3 \rightarrow O_2^- + O_2$	5.0×10^{9}	[77]
77	$O_3^- \rightarrow O_2 + O^-$	3.3×10^{3}	[77]
78	$O_3^- + H^+ \rightarrow O_2 + OH$	9.0×10^{10}	[77]
79	$HO_3 \rightarrow O_2 + OH$	1.0×10^{5}	[77]
80	$O + OH^- \rightarrow HO_2^-$	1.1×10^{5}	[77]
81	$H_2O_2 + O \rightarrow OH + HO_2$	1.6×10^{5}	[77]
82	$H_2O_2 \rightarrow 2OH$	2.3×10^{-7}	[77]
83	$O + HO_2^- \rightarrow OH + O_2^-$	5.3×10^{9}	[77]

Table 2 continued

No	Chemical Reactions	Rates [s^{-1}or $M^{-1}s^{-1}$]	Ref
84	$O_3 + H_2O_2 \rightarrow OH + HO_2 + O_2$	3.0×10^9	[77]

Rates for one-body, two-body, three body and four body reactions are in the unit of, respectively, s^{-1}, M^{-1} s^{-1}, M^{-2} s^{-1}, M^{-3} s^{-1}

The * is used to indicate reaction rates calculated from ionization rates in Ref. [79]

Appendix 3

See Table 3.

Table 3 Diffusion coefficients in liquid phase

Species	Diffusion coefficient (cm^2/s)	Reference
O	2.00×10^{-5}	[98]
$O(^1D)$	2.00×10^{-5}	[98]
$O_2(a)$	1.97×10^{-5}	[99]
O_3	1.75×10^{-5}	[100]
OH	2.30×10^{-5}	[101]
HO_2	1.00×10^{-5}	as H_2O_2
HO_3	1.00×10^{-5}	as H_2O_2
H_2O_2	1.00×10^{-5}	[102]
H_2	4.50×10^{-5}	[98]
H	4.50×10^{-5}	as H_2
e	1.00×10^{-1}	[103]
H^+	9.31×10^{-5}	[76]
OH^-	5.26×10^{-5}	[76]
HO_2^-	1.00×10^{-5}	as HO_2
O^-	2.00×10^{-5}	as O
O_2^-	1.97×10^{-5}	as O_2
O_3^-	1.75×10^{-5}	as O_3

Appendix 4

See Table 4.

Table 4 Maximum electric current and exposure time for human body [152]

Exposure time (min)	6	5	4	3	2	1	0.5
Contact RMS current (mA)	45	49	55	64	78	110	155

Appendix 5

See Table 5.

Table 5 Thermal and electrical parameters (at 13.56 MHz) of human skin tissues

Tissue type	Density (kg/m^3)	Thermal conductivity (W/mK)	Specific heat (J/kg K)	Metabolic heat (W/m^3)	Blood perfusion rate (ml/100 g min)	Relative permittivity	Electrical conductivity (S/m)
Skin	–	–	–	–	9.8	–	–
Stratum corneum	1500	0.235	3600	368.1	–	231.02	0.4069
Epidermis	1190	0.235	3600	368.1	–	210.68	1.82
Dermis	1116	0.445	3300	368.1	–	210.68	1.82
Hypodermis	971	0.185	2700	368.3	3.75	25.36	0.09
Muscle	4.1×10^6	0.385	–	67.0	2.71	138.44	0.83
Blood	1060	–	3770	–	–	–	–

Dielectric parameters (permittivity and conductivity) are calculated using the Cole–Cole model [148]. Thermal parameters for muscle and blood perfusion rate are from [149], and other thermal parameters are from [35]

References

1. Kong MG, Kroesen G, Morfill G, Nosenko T, Shimizu T, van Dijk J, Zimmermann JL (2009) New J Phys 11:115012
2. Fridman G, Friedman G, Gutsol A, Shekhter AB, Vasilets VN, Fridman A (2008) Plasma Process Polym 5(6):503
3. Ginsberg GG, Barkun AN, Bosco JJ, Burdick JS, Isenberg GA, Nakao NL, Petersen BT, Silverman WB, Slivka A, Kelsey PB (2002) Gastrointest Endosc 55(7):807
4. Isbary G, Morfill G, Schimidt HU, Georgi M, Ramrath K, Heinlin J, Karrer S, Landthaler M, Schimizu T, Steffes B, Bunk W, Monetti R, Zimmermann JL, Pompl R, Stolz W (2010) Br J Dermatol 163(1):78
5. Kim HH (2004) Plasma Process Polym 1(2):91
6. Locke BR, Sato M, Sunka P, Hoffmann MR, Chang JS (2006) Ind Eng Chem Res 45(3):882
7. Liston EM, Wertheimer MR, Martinu L (1993) J Adhes Sci Technol 7:1091
8. Siow KS, Britcher L, Kumar S, Griesser HJ (2006) Plasma Process Polym 3(6–7):392
9. Vleugels M, Shama G, Deng XT, Greenacre E, Brocklehurst T, Kong MG (2004) IEEE Trans Plasma Sci 33(2):824
10. Perni S, Liu DW, Shama G, Kong MG (2008) J Food Protect 71(2):302
11. Niemira BA (2012) J Food Sci 77(3):M171
12. Neumann E, Schaeferridder M, Wang Y, Hofschneider PH (1982) EMBO J 1(7):841
13. Aihara H, Miyazaki J (1998) Nat Biotech 16(9):867
14. Chalise PR, Perni S, Shama G, Novac BM, Smith IR, Kong MG (2006) Appl Phys Lett 89(15):153902
15. Gentile AC, Kushner MJ (1995) J Appl Phys 78(3):2074
16. Atkinson R, Baulch DL, Cox RA, Hampson RF, Kerr JA, Rossi MJ, Troe J (1997) J Phys Chem Ref Data 26(6):1329
17. Wang YH, Zhang YT, Wang DZ, Kong MG (2007) Appl Phys Lett 90:071501
18. Liu DX, Bruggeman P, Iza F, Rong MZ, Kong MG (2010) Plasma Sour Sci Technol 19(2):025018
19. Sakiyama Y, Graves DB, Chang H-W, Shimizu T, Morfill G (2012) J Phys D Appl Phys 45:425201
20. Murakami T, Niemi K, Gans T, O'Connell D, Graham WG (2013) Plasma Sour Sci Technol 22:015003
21. Van Gaens W, Bogaerts A (2013) J Phys D Appl Phys 46(7):275201
22. Walsh JL, Shi JJ, Kong MG (2006) Appl Phys Lett 89(16):161505
23. Reuter S, Winter J, Schmidt-Bleker A, Trsp H, Hammer MU, Weltmann KD (2012) IEEE Trans Plasma Sci 40(11):2788
24. Costerton JW, Stewart PS, Greenberg EP (1999) Science 284(5418):1318
25. Bergan T (1981) Rev Infect Dis 3(1):45
26. Tannock IF, Lee CM, Tunggal JK, Cowan DSM, Egorin MJ (2002) Clin Cancer Res 8(3):878
27. Zhang TC, Bishop PL (1994) Water Res 28(11):2267
28. Stewart PS (1996) Antimicrob Agents Chemother 40(11):3517
29. Wang CJ, Srivastava N, Dibble TS (2009) Appl Phys Lett 95(5):051501
30. Langer R (1998) Nature 392(6679):5
31. Babaeva NY, Kushner MJ (2010) J Phys D Appl Phys 43:185206
32. Babaeva NY, Ning N, Graves DB, Kushner MJ (2012) J Phys D Appl Phys 45:115203
33. Dower WJ, Miller JF, Ragsdale CW (1988) Nucleic Acids Res 16(13):6127
34. Coderre TJ, Katz J, Vaccarino AL, Melzack R (1993) Pain 52(3):259
35. Xu F, Lu TJ, Seffen KA (2008) J Mech Phys Solids 56(5):1852
36. Green DR, Reed JC (1998) Science 281:1309
37. Treybal RE (1980) Mass-transfer operations, 3rd edn. McGraw-Hill Kohakusha Ltd, Tokyo
38. Wust P, Hildebrandt B, Sreenivasa G, Rau B, Gellermann J, Riess H, Felix R, Schlag PM (2002) Lancet Oncol 3(8):487
39. Craig AD, Reiman EM, Evans A, Bushnell MC (1996) Nature 384:258
40. Li Z, Scheraga HA (1987) Proc Natl Acad Sci USA 84(19):6611
41. Kitano H (2002) Nature 420:206
42. Nielsen CB, Harper HA (1954) Exp Biol Med 86:753
43. Kingdon KH (1960) Phys Med Biol 5(1):1
44. Krueger AP, Andriese PC, Kotaka S (1963) Int J Biometeorol 7(1):3
45. Pratt R, Barnard RW (1960) Am Pharm Ass Sci Ed 49:643
46. Kellogg EW III, Yost MG, Barthakur N, Krueger AP (1979) Nature 281:400
47. Krueger AP, Reed EJ (1976) Science 193(4259):1209
48. Deng XT, Shi JJ, Kong MG (2007) J Appl Phys 101(7):074701

49. Fridman G, Shereshevsky A, Jost MM, Brooks AD, Fridman A, Gutsol A, Vasilets V, Friedman G (2007) Plasma Chem Plasma Process 27(2):163
50. Lee HJ, Shon CH, Kim YS, Kim S, Kim GC, Kong MG (2009) New J Phys 11:115026
51. Vandamme M, Robert E, Pesnel S, Barbosa E, Dozias S, Sobilo J, Lerondel S, Le Pape A, Pouvesle JM (2012) Plasma Process Polym 7(3–4):264
52. Park G, Ryu YH, Hong YJ, Choi EH (2012) Appl Phys Lett 100(6):063703
53. Krueger AP, Smith RF (1959) Nature 183:1332
54. Krueger AP, Smith RF, Gan Go Ing (1957) J Gen Physiol 41(2):359
55. Kanazawa S, Kogoma M, Moriwaki T, Okazaki S (1988) J Phys D Appl Phys 21(5):838
56. Lieberman MA, Lichtenberg AJ (2005) Principle of plasma discharges and materials processing, 2nd edn. Wiley, Hoboken
57. Lodish H, Berk A, Zipursky SL, Matsudaira P, Baltimore D, Darnell J (2000) Molecular cell biology, 4th edn. W. H. Freeman, New York
58. ArthroCare, http://phx.corporate-ir.net/phoenix.zhtml?c=100786&p=irol-newsArticle&ID=300673&highlight=. Accessed on September 21, 2013
59. PlasmaJet from Plasma Surgical, http://www.plasmasurgical.com/pdf/1.pdf. Accessed on September 21, 2013
60. Lewis WK, White WG (1924) Ind Eng Chem 16(12):1215
61. Higbie R (1935) Am Inst Chem Eng 31:365
62. Dankwertz PV (1951) Ind Eng Chem 43(6):1460
63. Yang AJ, Wang XH, Rong MZ, Liu DX, Iza F, Kong MG (2011) Phys Plasma 18(11):113503
64. Yuan X, Raja LL (2003) IEEE Trans Plasma Sci 31(4):495
65. Liu DW, Iza F, Kong MG (2008) Appl Phys Lett 93:261503
66. Wang Q, Economou DJ, Donnelly VM (2006) J Appl Phys 100:023301
67. Sakiyama Y, Graves DB (2009) Plasma Sources Sci Technol 18:025022
68. Shi JJ, Kong MG (2006) Phys Rev Lett 96:105009
69. Iza F, Lee JK, Kong MG (2007) Phys Rev Lett 99:075004
70. Liu DX, Rong MZ, Wang XH, Iza F, Kong MG, Bruggeman P (2010) Plasma Process Polym 7(9–10):846
71. Liu DX, Iza F, Wang XH, Kong MG, Rong MZ (2011) Appl Phys Lett 98(22):221501
72. Liu DX, Yang AJ, Wang XH, Rong MZ, Iza F, Kong MG (2012) J Phys D Appl Phys 45(30):305205
73. Stewart PS (2003) J Bacteriol 185(5):1485
74. Stewart PS (1998) Biotechnol Bioeng 59:261
75. Klapper I, Dockery J (2010) SIAM Rev 52(2):221
76. Buettner G and Mason RP, Critical Rev. Oxidative Stress and Aging: Advances in Basic Science, Diagnostics, and Intervention (2003) Ed Cutler RG and Rodriguez, World Scientific, New Jersey, London, Singapore, Hong Kong, vol. 1, Chapter 2, pp. 27–38
77. Newman JS (1973) Electrochemical systems. Prentice-Hall, Englewood Cliffs
78. Cents AHG, Brilman DWF, Versteeg GF (2005) Chem Eng Sci 60:5830
79. Pastina B, LaVerne JA (2001) J Phys Chem A 105:9316
80. Barat F, Gilles L, Hickel B, Lesigne B (1971) J Phys Chem 75(14):2177
81. Schweitzer C, Schmidt R (2003) Chem Rev 103:1685
82. Heikes BG (1984) Atmos Environ 18(7):1433
83. He ZG, Liu JS, Cai WM (2005) J Electrostat 63:371
84. Emfietzoglou D, Nikojoo HA (2007) Radiat Res 167(1):110
85. Wizke M, Rumbach P, Go DB, Sankaran RM (2012) J Phys D Appl Phys 45:442001
86. Walsh JL, Liu DX, Iza F, Rong MZ, Kong MG (2010) J Phys D Appl Phys 43(3):032001
87. Eyring H (1936) J Chem Phys 4:283
88. Newman JS (1973) Electrochemical systems. Prentice-Hall, Englewood Cliffs
89. Dobrynin D, Arjunan K, Fridman A, Friedman G, Clyne AM (2011) J Phys D Appl Phys 44:075201
90. Boxhammer V, Morfill GE, Jokipii JR, Shimizu T, Klampfl T, Li Y-F, Koritzer J, Schlegel J, Zimmermann JL (2012) New J Phys 14:113042
91. Lee HWK, Lee HW, Kang SK, Kim HY, Won IH, Jeon SM, Lee JK (2013) Plasma Sources Sci Technol 22:055008
92. Kong MG, MRS Spring 2012; Kong GEC 2012; Kushner MJ, ICOPS 2013; Kong MG, ISPC 2013
93. Whitman WG (1923) Chem Met Eng 29:147
94. Krishna R, Standart GL (2010) A I Ch E J 22(2):383
95. Higbie R (1935) Trans Am Inst Chem Eng 31(2):365
96. Mackay D, Shiu WY (1981) J Phys Chem Ref Data 10(4):1175
97. Sotelo JL, Beltran FJ, Benitez FJ, Beltran-Heredia J (1989) Water Res 23(10):1239

98. Blauwhoff PMM, Versteeg GF, van Swaaij WPM (1984) Chem Eng Sci 39(2):207
99. Stewart PS (2003) J. Bacteriol 185(5):1485
100. Richard T Cornell composting files, science and engineering, calculating the oxygen diffusion coefficient in water, http://compost.css.cornell.edu/oxygen/oxygen.diff.water.html, accessed on September 22, 2013
101. Gong XB, Takagi S, Huang HX, Matsumoto Y (2007) Chem Eng Sci 62(4):1081
102. Svishchev IM, Plugatyr AY (2005) J Phys Chem B 109:4123
103. Zhang JJ, Oloman CW (2005) J Appl Electrochem 35:945
104. Kahlert H, Retter U (1998) J Phys Chem 102:8757
105. Nedeltchev S, Jordan U, Schumpe A (2007) Chem Eng Sci 62:6263
106. Limtrakul S, Kongto A, Vatanatham T, Ramachandran PA (2010) Chem Eng Sci 65(15):4420
107. Marchello JM, Toor HL (1963) Ind Eng Chem 2(1):8
108. Toor HL, Marchello JM (1958) A I Ch E J 4(1):97
109. Sieck LW, Herron JT, Green DS (2000) Plasma Chem Plasma Process 20:235
110. Molina-Cuberos GJ, Lopez-Moreno JJ, Rodrigo R, Lichtenegger H, Schwingenschuh K (2001) Adv Space Res 27(1):1801
111. Lindinger W, Albritton DL (1975) J Chem Phys 62:3517
112. Shi JJ, Liu DW, Kong MG (2006) Appl Phys Lett 89:081502
113. Liu JJ, Kong MG (2011) J Phys D Appl Phys 44(34):345203
114. Vroom JM, De Grauw KJ, Gerritsen HC, Bradshaw DJ, Marsh PD, Watson GK, Birmingham JJ, Allison C (1999) Appl Environ Microbiol 65(8):3502
115. Sander R (1999) Compilation of Henry's law constants for inorganic and organic species of potential importance in environmental chemistry (Version 3). http://www.henrys-law.org. Accessed in Nov 2008
116. Perry's Chemical Engineers' Handbook, P173
117. Orazov M, Sakiyama Y, Graves DB (2012) J Phys D Appl Phys 45:445201
118. Deng S, Ruan R, Mok CK, Huang G, Lin X, Chen P (2007) J Food Sci 72(2):M62
119. Perni S, Shama G, Kong MG (2008) J. Food Protect 71(8):1619
120. Ragni L, Berardinelli A, Vannini L, Montanari C, Sim F, Guerzoni ME, Guarnieri A (2010) J Food Eng 100(1):125
121. Noriega W, Shama G, Laca A, Diaz M, Kong MG (2011) Food Microbiol 28(7):1293
122. Dobrynin D, Fridman G, Friedman G, Fridman A (2009) New J Phys 11:115020
123. Lademann J, Kramer A, Weltmann KD, Hartmann B, Fluhr JW, Hinz P, Hubner G, Lademann O, Ottomann C, Richter H, Alborova A, Humme D, Patzelt A (2009) J. Biomed Optics 14(5):054025
124. Lademann J, Ulrich C, Richter H, Kluschke F, Lademann O, Kramer A, Weltmann KD, Lange-Asschenfeldt B (2013) Clin Plasma Med 1:5
125. Foster KR (2000) IEEE Trans Plasma Sci 28(1):15
126. Chichel A, Skowronek J, Kubasewska M, Kanikowski M (2007) Rep Pract Radiother 12(5):267
127. Pennes HH (1948) J Appl Physiol 1:93
128. Xu F, Lu TJ, Seffen KA (2008) Acta Mech Sinica 24:1
129. Edd JF, Horowitz L, Davalos RV, Mir LM, Rubinsky B (2006) IEEE Trans Biomed Eng 53(5):1409
130. Lee RC (1997) Curr Probl Surg Sep 34(9):677
131. Lee RC and Astumian RD (1996) 22(7): 509
132. Weaver JC, Chizmadzhev Yu A (1996) Bioelectrochem Bioenetics 41(2):135
133. Marrink SJ, de Vries AH, Tieleman DP (2009) Biochim Biophys Acta Biomembr 1788(1):149
134. Joshi RP, Schoenbach KH (2000) Phys Rev E 62(1):1025
135. Vernier PT, Ziegler MJ, Sun Y, Chang W, Gundersen MA, Tieleman DP (2006) J Am Chem Soc 128(9):6288
136. Hu Q, Zhang Z, Kong MG, Joshi RP (2013) Phys Rev E 87(3):032704
137. Shao Y et al (2006) Phys Chem Chem Phys 8(27):3172
138. Henzler-Wildman KA, Lei M, Thai V, Kerns SJ, Karplus M, Kern D (2007) Nature 450:913
139. Kamerlin SCL, Warshel A (2009) Proteins Struct Funct Bioinform 78(6):1339
140. Chang IA, Nguyen UD (2004) Biomed Eng Online 3:27
141. Kosturski N, Margenov S, Vutov Y (2012) AIP Conf Proc 1497:120
142. Henriques FC, Moritz AR (1947) Am J Pathol 23:531
143. Berjano EJ (2006) BioMed Eng OnLine 5:24
144. Park J, Henins I, Herrmann HW, Selwyn GS (2001) J Appl Phys 89(1):15
145. Walsh JL, Zhang YT, Iza F, Kong MG (2008) Appl Phys Lett 93(22):221505
146. Yang AJ, Rong MZ, Wang XH, Liu DX, Kong MG (2013) J Phys D Appl Phys 46(41):415201
147. Sakiyama Y, Graves DB (2006) J Phys D Appl Phys 39:3644

148. Gabriel S, Lau RW, Gabriel C (1996) Phys Med Biol 41:2271
149. Diller KR (1994) Ann N Y Acad Sci 720:38
150. D'Ambrosio V, Dughiero F (2007) Med Bio Eng Comput 45:459
151. Kurgan E, Gas P (2011) PREEGLAD ELECKTROTECHINCZNY 87(12b):103
152. Safety Code 6 Regulation, Limits of human exposure to radio frequency electromagnetic fields in the frequency range from 3 kHz to 300 GHz, Health Canada HC Pub: 091029, 2009
153. Deng XT, Shi JJ, Kong MG (2006) IEEE Trans Plasma Sci 34(4):1310
154. Deng XT, Shi JJ, Chen HL, Kong MG (2007) Appl Phys Lett 90(1):013903
155. Ellerweg D, Benedikt J, von Keudell A, Knake N, Schulz-von der Gathern V (2010) New J Phys 12(1):013021
156. Waskoenig J, Niemi K, Knake N, Graham LM, Reuter S, Schulz-von der Gathern V, Gans T (2010) Plasma Sour Sci Technol 19(4):045018
157. O'Connell D, Cox LJ, Hyland WB, McMahon SJ, Reuter S, Graham WG, Gans T, Currell FJ (2011) Appl Phys Lett 98(4):043701
158. Lissi EA, Encinas MV, Lemp E, Rubio MA (1993) Chem Rev 93(2):699
159. Schweitzer C, Schmidt R (2003) Chem Rev 103(5):1685
160. Ionin AA, Kochetov IV, Yuryshev NN (2007) J Phys D Appl Phys 40(2):R25
161. Sousa JS, Bauville G, Lacour B, Puech V, Touzeau M, Pitchford LC (2008) Appl Phys Lett 93(10):011502
162. Yusupov M, Neyts EC, Simon P, Bergiyorov G, Snoeckx R, van Duin ACT, Bogaerts A (2014) J Phys D Appl Phys 47:025025
163. Yusupov M, Bogaert A, Huygh S, Snoeckx R, van Duin ACT, Neyts EC (2013) J Phys Chem C 117:5993
164. Fridovich I (1978) Science 201(4):875
165. Reaume AG, Elliott JL, Hoffman EK, Kowall NW, Ferrante RJ, Siwek DR, Wilcox HM, Flood DG, Beal MF, Brown RH Jr, Scott RW, Snider WD (1996) Nat Genet 13:43
166. Yang AJ, Rong MZ, Wang XH, Liu DX, Kong MG (2013) J Phys D Appl Phys 46(41):415201
167. Pryor WA (1986) Ann Rev Physiol 48:657
168. Behl C, Davis JB, Lesley R, Schubert D (1994) Cell 77(6):817
169. Imlay JA (2008) Ann Rev Biochem 77:755
170. Janero DR (1990) Free Radic Biol Med 9(6):515
171. Gutteridge JMC (1995) Clin Chem 41(12):1819
172. Stewart PS, Peyton BM, Drury WJ, Murga R (1993) Appl Environ Microbiol 59(1):327
173. Rittmann BE, McCarty PL (1980) Biotechnol Bioeng 22:2343
174. Davies DG, Parsek MR, Pearson JP, Iglewski BH, Costerton JW, Greenberg EP (1998) Science 280:295
175. Heydorn A, Nielsen AT, Hentzer M, Sternberg C, Givskov M, Ersboll BK, Molin S (2000) Microbiology 146:2395
176. Kong MG, Deng XT, Shi JJ, Shama G, Greenacre E and Buckhurst T, presented at ElectroMed 2005 Symposium, May 15–18, 2005, Portland, Oregon, USA
177. Xiong ZL, Du TF, Lu XP, Cao YG, Pan Y (2011) Appl Phys Lett 98:221503
178. Imlay JA, Linn S (1986) J Bacteriol 166:519
179. Otero MC, Nader-Macias ME (2006) Anim Reprod Sci 96:35
180. Broadwater WT, Hoehn RC, King PH (1973) Appl Microbiol 26:391
181. Pei X, Lu X, Liu J, Liu D, Yang Y, Ostrikov K, Chu PK, Pan Y (2012) J Phys D Appl Phys 45:165205
182. Ikawa S, Kitano K, Hamaguchi S (2009) Plasma Process Polym 7(1):33
183. Balcon N, Aanesland A, Boswell R (2007) Plasma Sour Sci Technol 16(2):217
184. Shi JJ, Zhang J, Qiu G, Walsh JL, Kong MG (2008) Appl Phys Lett 93(4):041502
185. Li WP, Zhu MS et al (2006) Burn 32:986
186. Eden JG, Park S-J, Ostrom NP, McCain ST, Wagner CJ, Vojak BA, Chen J, Liu C, von Allmen P, Zenhausern F, Sadler DJ, Jensen C, Wilcox DL, Ewing JJ (2003) J Phys D Appl Phys 36(23):2869
187. Cao Z, Nie Q, Bayliss DL, Walsh JL, Ren CS, Wang DZ, Kong MG (2010) Plasma Sour Sci Technol 19(2):025003
188. Graves DB (2012) J Phys D Appl Phys 45(26):263001
189. Stamler JS, Singel DJ, Loscalzo J (1992) Science 258(5090):1898
190. Richmonds C, Sankaran RM (2008) Appl Phys Lett 93(13):131501
191. Li J, Sato M, Ohshima T (2007) Thin Solid Films 515(9):4283